UNIVERSITY OF BIRMINGHAM
University of Birmingham Research at Birmingham

Active screen plasma nitriding of Fe-24Mn-2Al-0.45C TWIP steel

Tao, Xiao; Collins, Thomas John; Ao, Qingshuo; Liu, Huibin; Dashtbozorg, Behnam; Li, Xiaoying; Dong, Hanshan

DOI:
10.1016/j.actamat.2022.118418

License:
Creative Commons: Attribution (CC BY)

Document Version
Publisher's PDF, also known as Version of record

Citation for published version (Harvard):
Tao, X, Collins, TJ, Ao, Q, Liu, H, Dashtbozorg, B, Li, X & Dong, H 2022, 'Active screen plasma nitriding of Fe-24Mn-2Al-0.45C TWIP steel: microstructure evolution and a synergistic selective oxidation mechanism', *Acta Materialia*, vol. 241, 118418. https://doi.org/10.1016/j.actamat.2022.118418

Link to publication on Research at Birmingham portal

General rights
Unless a licence is specified above, all rights (including copyright and moral rights) in this document are retained by the authors and/or the copyright holders. The express permission of the copyright holder must be obtained for any use of this material other than for purposes permitted by law.

•Users may freely distribute the URL that is used to identify this publication.
•Users may download and/or print one copy of the publication from the University of Birmingham research portal for the purpose of private study or non-commercial research.
•User may use extracts from the document in line with the concept of 'fair dealing' under the Copyright, Designs and Patents Act 1988 (?)
•Users may not further distribute the material nor use it for the purposes of commercial gain.

Where a licence is displayed above, please note the terms and conditions of the licence govern your use of this document.

When citing, please reference the published version.

Take down policy
While the University of Birmingham exercises care and attention in making items available there are rare occasions when an item has been uploaded in error or has been deemed to be commercially or otherwise sensitive.

If you believe that this is the case for this document, please contact UBIRA@lists.bham.ac.uk providing details and we will remove access to the work immediately and investigate.

Download date: 28. Apr. 2024

Acta Materialia 241 (2022) 118418

Contents lists available at ScienceDirect

Acta Materialia

journal homepage: www.elsevier.com/locate/actamat

Active screen plasma nitriding of Fe-24Mn-2Al-0.45C TWIP steel: Microstructure evolution and a synergistic selective oxidation mechanism

Xiao Tao[a,*], Thomas John Collins[a], Qingshuo Ao[a], Huibin Liu[b], Behnam Dashtbozorg[a], Xiaoying Li[a], Hanshan Dong[a]

[a] School of Metallurgy and Materials, University of Birmingham, Birmingham B15 2TT, UK
[b] Baoshan Iron & Steel Co., Ltd, Shanghai 201900, PR China

ARTICLE INFO

Article history:
Received 24 April 2022
Revised 29 September 2022
Accepted 4 October 2022
Available online 5 October 2022

Keywords:
Plasma nitriding
Selective oxidation
Active screen plasma
TWIP steel
Expanded austenite
Surface hardening

ABSTRACT

In this study, Fe-24Mn-2Al-0.45C twinning-induced plasticity (TWIP) steel was investigated after active screen plasma nitriding (ASPN) at 350–480 °C. Up to 450 °C, the ASPN-treated TWIP steel showed a double-layered structure, with a topmost Fe_4N-type γ' layer and an underlying interstitial solid solution. The underlying nitrogen interstitial solid solution obtained on ASPN-treated TWIP steel can be identified as $\gamma_{N(i)}$, being expanded austenite with small lattice expansions at low nitrogen (and carbon) absorption levels. However, the 480 °C ASPN-treated TWIP steel surface is composed of an unexpected MnO-containing ferritic topmost layer and a thick underlying $\gamma_{N(i)}$ layer, which corresponds to a hardness-depth profile different to those obtained at 350–480 °C. Hence, we propose and elucidate a selective oxidation mechanism (that occurred alongside nitrogen inward diffusion) on TWIP steel during ASPN treatment, which can be attributed to (a) an elevated treatment temperature that allowed Mn migration, (b) a processing atmosphere with low oxygen partial pressure, and (c) a high-Mn substrate chemical composition with low Al/Mn (or Si/Mn) ratio.

© 2022 The Authors. Published by Elsevier Ltd on behalf of Acta Materialia Inc.
This is an open access article under the CC BY license (http://creativecommons.org/licenses/by/4.0/)

1. Introduction

Since the early 1980s, low-temperature plasma nitriding has been studied and developed for austenitic stainless steels (ASSs) to improve material surface hardness and wear resistance with no loss of (in some cases, improved) corrosion properties [1–4]. The enhancement in surface properties is due to the formation of nitrogen interstitially supersaturated surface layer on ASSs. The low nitriding treatment temperatures (< 450 °C) enable inward diffusion of interstitial elements in the absence of segregation of large substitutional elements [5]. After the accommodation of extremely high (or "colossal" [6–8]) quantities of nitrogen, the original face-centered cubic (FCC) structure experiences a characteristic anisotropic lattice expansion, which comes to the terminology of nitrogen-expanded austenite, γ_N (also known as S-phase) [8–15]. Cr is considered an essential element for nitrogen-supersaturation, which was hypothesised to be achieved via "trapping" of N by Cr atoms, thereby forming short-range ordered Cr-N "clusters" [16–20]. Martinavicius et al. [21,22] reported local Cr/N rich regions in γ_N, which has led to the consideration of spinodal decomposition in γ_N at typical low nitriding treatment temperature [23,24]. Nitrogen-supersaturated expanded austenite is known to form on the surface of various Cr-containing corrosion-resistant alloys (i.e. Fe-Cr-Ni/Mn, Co-Cr and Ni-Cr systems, as reviewed in Ref. [18]).

Despite the significant effort dedicated to nitrogen-supersaturation of high-Cr substrates, little attention has been paid to the low-temperature thermochemical diffusion treatment of Cr-free Mn/Ni-stabilised austenitic steels. Following a study on triode-plasma nitriding (TPN) for a non-stainless Fe-36Ni and a Fe-19Cr-35Ni ASS alloy at 400–450 °C [25], a high Cr content in the substrate alloy plays a pivotal role in colossal interstitial-supersaturation, but not a necessity for the development of the nitrogen-induced lattice expansion. Increases in Cr content from 0 to 17.66 wt% in Fe-Cr-Ni systems (at a constant ~27 wt% Ni) can enhance surface nitrogen absorption upon plasma nitriding at 380 °C [26].

As reviewed by Cooman et al. [27], high-Mn austenitic twinning-induced plasticity (TWIP) steels – with the typical composition of 15–30 wt% Mn, <1 wt. % C, <3 wt% Al and <3 wt%

* Corresponding author.
E-mail addresses: x.tao@bham.ac.uk, hugou2008@hotmail.com (X. Tao).

https://doi.org/10.1016/j.actamat.2022.118418
1359-6454/© 2022 The Authors. Published by Elsevier Ltd on behalf of Acta Materialia Inc. This is an open access article under the CC BY license (http://creativecommons.org/licenses/by/4.0/)

Si – have drawn extensive interest for their unique strain hardening behavior and a good combination of mechanical properties for automotive, cryogenic storage, and non-magnetic structural applications. Despite their high ultimate tensile strength and good strength-ductility balance, austenitic TWIP steels possess relatively low yield strengths and can exhibit poor wear and corrosion performance. Thermochemical nitrogen diffusion treatment has the potential to enhance the poor wear and corrosion performance of Cr-free, high-Mn TWIP steel.

Given the chemical composition of TWIP steel (i.e. no/low Cr, high-Mn and low-Al content), a relatively thick "less-expanded" expanded austenite (as reported on Fe-36Ni Invar [25]) is anticipated after low-temperature plasma nitriding treatments. Firstly, a "non-stainless" steel substrate tends to have a thicker treatment layer than its stainless counterpart after equivalent low-temperature nitriding treatment at ~400–450 °C (i.e., ~10–25 μm on Fe-36Ni, and ~4–14 μm on Fe-19Cr-35Ni) [25]. Secondly, the Al alloying content in TWIP steel tends to promote nitrogen absorption and might act as a "nitrogen-trapper" similar to that of Cr, since both Cr and Al are strong nitride-forming elements in steel. Thirdly, compared to high-Ni ASSs, Mn-stabilised ASSs tend to possess higher nitrogen absorption, larger 'apparent' lattice expansions and higher surface hardness following plasma nitriding treatments [28–32]. The high Mn content in TWIP steels can enhance N interstitial solubility.

Al-addition in steels can be beneficial for reduced density (~1.3% reduction in density per 1 wt% Al addition [33]). However, high Al addition (and high C content) in TWIP steel can lead to κ-carbide precipitation and destabilisation of austenite during heat treatments (as reviewed by Chen et al. [34]). Given this consideration, low-Al medium-C TWIP steel was selected and investigated in this study to avoid the destabilisation of austenite during systematic nitriding treatments between 350 and 480 °C. This study paves the way toward industrial implementations of plasma surface engineering technologies for high-Mn steels and provides new insights for nitrogen interstitial 'expandable' engineering steels.

2. Experimental

2.1. Material and surface treatments

TWIP steel with nominal composition, Bal. Fe, 24 wt% Mn, 2 wt% Al, 0.45 wt% C and 0.05 max wt% Si, was received and prepared to ~25 × 25 × 3 mm plates. One side of the plate was ground successively using P400, P800 and P1200 SiC paper. Ground plates were ultrasonically cleaned in acetone for 15 mins. Active screen plasma nitriding (ASPN) was carried out for 10 h at 350, 400, 450 and 480 °C using an industrial Plasma Metal active screen plasma unit. For comparison, AISI 316 stainless steel samples (with nominal composition, Bal. Fe, 18 wt% Cr, 11 wt% Ni, 3 wt% Mo) were also prepared and treated at 450 and 480 °C for 10 h under equivalent ASPN conditions. A previous study on ASPN treatment of AISI 316 ASS (using the same plasma unit) can be found in Ref. [35]. Sample denotation in this study is based on treatment temperature and material. For example, N450-ASS and N450-TWIP denote the AISI 316 ASS and the TWIP steel samples nitrided at 450 °C for 10 h, respectively.

During ASPN treatments, the prepared TWIP steel samples and two stainless steel 'dummy' samples (each inserted with a type K thermocouple for measuring and controlling temperatures during treatment) were placed on a 1.4 m diameter worktable in a 2 m tall vacuum chamber, which was then evacuated to below 0.01 mbar. The active screen was made of AISI 316 ASS. ASPN were all carried out at 0.75 mbar in 25% N_2 + 75% H_2 gas mixture. The worktable was connected to low electrical power at 0.75 kVA. The active screen was applied with a separate electrical power at 15–25 kVA, depending on the target treatment temperature at 350–480 °C. After treatment, cooling was carried out under vacuum at ~0.8 mbar before ventilation to atmospheric pressure at temperatures below ~100 °C.

In contrast to conventional direct current (DC) plasma nitriding (where specimens are negatively biased and act as the cathode), an independent mesh cage (known as the active screen) acts as the cathode and the specimens are normally held at floating potential (or applied with a small negative bias) under ASPN [35–37]. In this way, ion bombardment, cathodic sputtering and arc formations are redirected away from the sample to the active screen during ASPN. The increase in treatment temperature during ASPN is primarily achieved by the thermal radiant heating from the active screen, which requires higher electric power applied on the active screen (instead of workpiece). It is worth mentioning that, following ASPN treatment using a stainless-steel active screen, nanoparticle deposition of Fe_xN can be observed on the sample surfaces, which is owing to material transfer via a "sputtering (from the active screen) and deposition (onto the sample surface)" mechanism [37–40]. When the stainless-steel screen is integrated (or replaced) with other materials in the case of ASP surface functionalisation treatments, depositions other than iron-nitrides can be achieved on metallic [41–43] and C-based materials (as reviewed in [44]) for enhanced electric properties.

2.2. Material characterisation and evaluation

X-ray diffraction (XRD) analysis was carried out using a PROTO AXRD benchtop diffractometer (Cu-Kα, 0.154 nm). The 2-Theta scanning angle, step and dwell time are 30–80 °, 0.015 ° and 2 s, respectively. The elemental depth profiles were investigated via glow discharge optical emission spectroscopy (GDOES) using a Spectruma GDA650HR instrument. Sample cross-sections were prepared and etched in 5% Nital (vol%) for TWIP steel and 50HCl-25HNO_3-25H_2O (vol%) for AISI 316 stainless steel.

Scanning electron microscopy (SEM) images were taken from an FEI Quanta 3D microscope. Layer thicknesses were measured from etched sample cross-sections under SEM. Cross-sectional transmission electron microscopy (TEM) samples were extracted from the top of treated surfaces and thinned using an FEI Quanta 3D instrument under a 30 kV Ga^+ ion beam. TEM samples were then examined under a Jeol 2100 microscope (LaB_6, 200 kV) and a Philips Tecnai F20 microscope (FEG, 200 kV). Scanning TEM (STEM) and high angle annular dark-field (HAADF) imaging was performed under a Philips Tecnai F20 microscope.

Nanoindentation hardness was evaluated on sample cross-sections under depth control mode (constant indent depth at ~200 nm) using a Micro Materials NanoTest Vantage instrument, equipped with a diamond Berkovich indenter. The load-depth data were processed based on the Oliver–Pharr method. The displacement from surface for each indent was measured under SEM. Surface Vickers micro-hardness was evaluated using a Mitutoyo MVK-H1 hardness indenter at an indentation load of 0.025 kg and a dwell time of 10 s. The mean hardness values ± standard deviations were evaluated from at least 8 indents made at random locations on top of sample surfaces.

3. Results

3.1. Surface morphology and layer thickness

Fig. 1 shows the top-view surface morphology for TWIP steel after ASPN. The nano-particles observed following ASPN are most likely iron nitrides, Fe_xN, formed via a "sputtering and deposition" mechanism, which typically refers to material transfer from the active screen unit [37–40]. The increased number density of Fe_xN

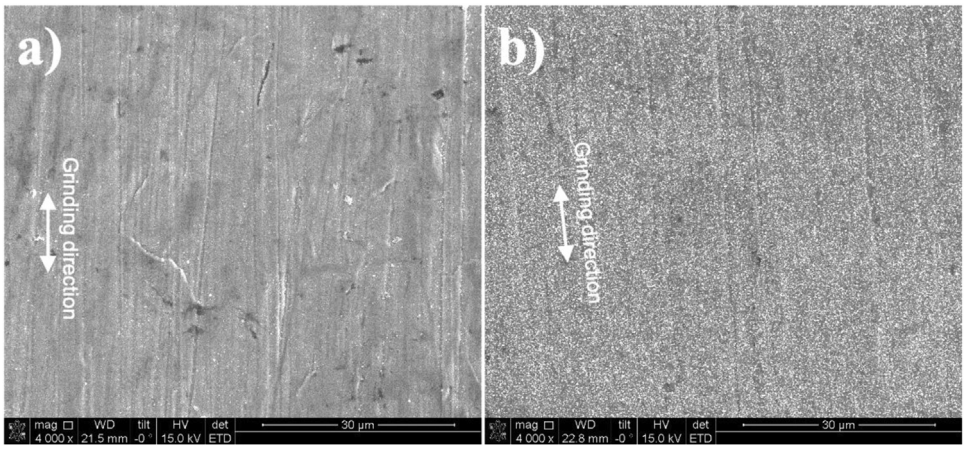

Fig. 1. SEM images showing the surface morphology of TWIP steel after ASPN at 450 °C (a) and (b) 480 °C.

Table 1
Layer thicknesses (measured from etched cross-sections) and surface hardness; data are presented as mean ± standard deviation.

	Layer thickness, μm		Surface hardness, $HV_{0.025}$
	Top layer	Total layer	
UNT-TWIP	/	/	310 ± 17
N350-TWIP	1.4 ± 0.3	2.4 ± 0.1	555 ± 68
N400-TWIP	3.3 ± 0.6	7.0 ± 0.3	892 ± 37
N450-TWP	6.2 ± 0.9	12.5 ± 0.6	1275 ± 95
N480-TWIP	0.7 ± 0.2	13.2 ± 1.5	738 ± 39
UNT-ASS	/	/	239 ± 9
N450-ASS	/	10.3 ± 1.1	1342 ± 116
N480-ASS	/	13.3 ± 1.3	1464 ± 111

nanoparticles at elevated treatment temperature (Fig. 1b) is consistent with the higher electric power applied (and more sputtering) on the active screen for achieving/maintaining a higher treatment temperature. Noticeably, the abrasive grooves introduced during sample grinding were still observed after ASPN, which demonstrates limited cathodic sputtering on workpice during the ASPN treatment.

Fig. 2 shows the cross-sectional layer morphology after etching. A single layer was seen on both N450-ASS and N480-ASS (Fig. 2a and b) with a clear interface to the underlying material core. Dark regions were seen at the top of the treated layer on N480-ASS (Fig. 2b), which can be attributed to the local decomposition of γ_N with CrN precipitation forming at the higher treatment temperature. In contrast, TWIP steel showed a double-layered morphology after ASPN treatments (Fig. 2c–f), where a sharp interface can be observed between the topmost layer and the underlying layer, suggesting different phase compositions (see Section 3.4).

Layer thicknesses were measured from etched sample cross-sections and presented in Table 1. In general, the thickness of the total treatment layer on TWIP steel increases with increasing treatment temperature after ASPN at 350–480 °C. However, different to the consistent increase in layer thickness with treatment temperature (for both the topmost layer and the total layer) for TWIP steel treated at 350–450 °C, the thickness of the topmost layer drops sharply from ~6.6 μm on N450-TWIP to ~0.7 μm on N480-TWIP, which could be associated to the change in surface phase composition. After ASPN at 450 °C, the treatment layer obtained on TWIP steel appear to be thicker than those formed on ASS (cf. ~12.5 μm on N450-TWIP and ~10.3 μm on N450-ASS). However, at an elevated treatment temperature of 480 °C, N480-TWIP and N480-ASS showed a similar total layer thickness at ~13 μm.

3.2. Composition depth distribution

The composition-depth distribution was investigated using GDOES and the results are shown in Fig. 3. Similar to the nitrogen-expanded austenite layers reviewed in [15,18], the nitrogen profile for N450-ASS shows a gradual decline across the treatment layer and an abrupt drop at the layer/substrate interface (Fig. 3a). In contrast, corresponding to the double-layered morphology observed on TWIP steel after ASPN at 350–450 °C (Fig. 2c–e), GDOES curves in Fig. 3c–e reveal a topmost high-nitrogen region and an underlying low-nitrogen region, with the latter exhibiting a rather long "tail" of gradually reducing nitrogen content towards the core. A change in the gradient of nitrogen profiles (or nitrogen "shoulder") can be identified in Fig. 3c–e at the interface between the topmost and the underlying layer. As indicated by the vertical dashed lines in Fig. 3c–e, these "N shoulders" locate at 1.3 μm for N350-TWIP, 3.1 μm for N400-TWIP, and 5.7 μm for N450-TWIP, which agree with the top layer thicknesses measured from the etched sample cross-sections, i.e., at 1.4 μm, 3.3 μm and 6.2 μm, respectively (Table 1).

A carbon hump is observed at the nitrogen front on ASS after ASPN at both 450 and 480 °C (Fig. 3a and b), which is attributable to carbon atoms being pushed inward under the nitrogen inward diffusion. A similar C hump can be identified at the end of the total treatment layer on TWIP steel after ASPN at 350–450 °C in Fig. 3c–e. Intriguingly, and consistent with the double-layered structure, an additional C hump can be seen at the interface between the two layers on ASPN-treated TWIP steels. This additional C hump is seen at approximately the same depth as the abovementioned N "shoulder". For TWIP steels after ASPN at 350–450 °C, C content seems depleted at the topmost layer before increasing towards the first hump (Fig. 3c–e). In the underlying layer, C content was found at an intermediate level > 1.4 at% (> ~0.3 wt%), which increased to a level greater than 2.0 at% at the second C hump, before gradually recovering towards 2.0 at% (~0.45 wt%) within the unmodified core. In agreement with ASS, carbon atoms at the surface of TWIP steel also appeared to be pushed inward under the influence of nitrogen inward diffusion. No significant concentration variation is noticed for Fe, Al and Mn for TWIP steel after ASPN treatments at 350-450 °C.

Compared to the TWIP steels treated between 350 and 450 °C (Fig. 3c–e), N480-TWIP shows a thicker total nitrogen layer depth (for a higher treatment temperature employed), but at much lower nitrogen concentration levels. The 0.8 μm thick topmost region on N480-TWIP (as indicated in Fig. 3f) corresponds to the thin surface layer in Fig. 2f. The thick underlying layer on N480-TWIP (Fig. 2f)

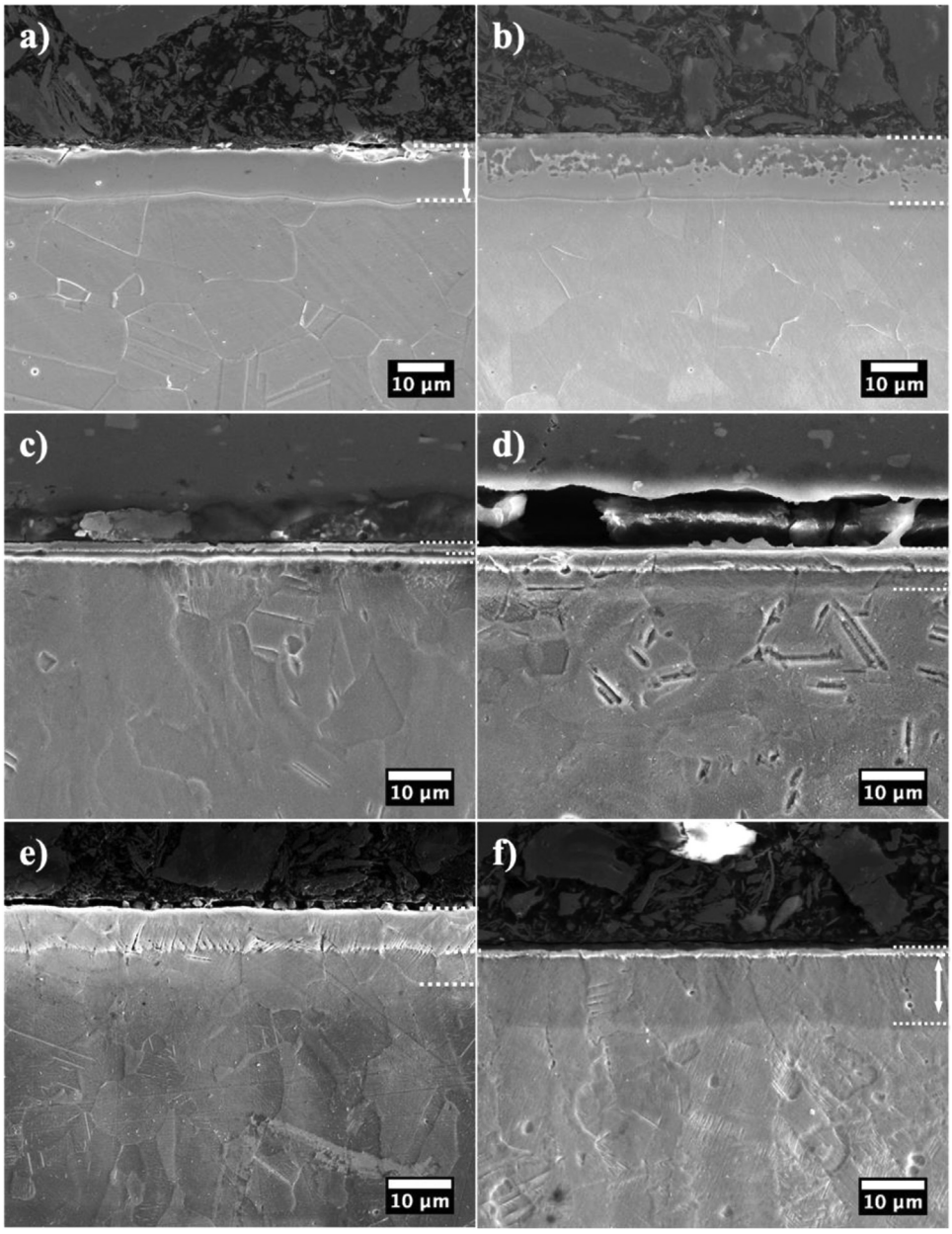

Fig. 2. SEM images showing the treatment layers cross-sectionally on AISI 316 ASS (etched in 50HCl-25HNO_3-25-H_2O, vol%) after ASPN treatments: (a) N450-ASS, (b) N480-ASS; compared to TWIP steel (etched in 5% Nital) after ASPN treatments: (c) N350-TWIP, (d) N400-TWIP, (e) N450-TWIP, and (f) N480-TWIP.

shows a long "tail" of gradually reducing nitrogen content towards the unmodified core (Fig. 3f). Two C humps were also found on N480-TWIP in Fig. 3f, where the topmost layer exhibits the lowest C content at > 0.7 at% and the underlying layer shows an intermediate carbon level of > 1.2 at% (in contrast to 2 at% C for the unmodified substrate). Most importantly, within the 0.8 μm thick topmost layer on N480-TWIP, Fig. 3f shows (i) Fe "peak" and Mn "valley" (with the highest point of Fe and the lowest point of Mn at the same depth of ~0.4 μm) and (ii) a "flattened" N profile and a "valley" in C profile, indicating a surface phase composition different to those at 350–450 °C (see further discussion in Section 4.3).

3.3. Surface hardening

Surface hardness values are presented in Table 1. Consistent with the increase in layer depth, the surface hardness of TWIP steel increases with treatment temperature from ~555 $HV_{0.025}$ at 350 °C to ~1275 $HV_{0.025}$ at 450 °C. The surface hardness of N450-TWIP at ~1275 $HV_{0.025}$ is at a similar level to N450-ASS at 1342 $HV_{0.025}$. However, compared to the further increase in surface hardness for ASPN-treated ASS from ~1342 $HV_{0.025}$ at 450°C to ~1464 $HV_{0.025}$ at 480 °C, the surface hardness of ASPN-treated TWIP drops to ~738 $HV_{0.025}$ at 480 °C, which associates well with the change in nitrogen absorption as shown in Fig. 3e&f.

The cross-sectional nanoindentation hardness-depth profiles are shown in Fig. 4. The hardness-depth profiles for N450-TWIP and N480-TWIP agree with the double-layered morphologiesin Fig. 2e&f and the nitrogen composition-depth distributions in Fig. 3e&f. N450-TWIP shows (a) high hardness values above ~10 GPa at the topmost surface at depths < 6.7 μm, and (b) a sharp drop in hardness from 9.4 to 6.9 GPa between the depths of 6.7–8.2 μm (Fig. 4). Such hardness profile correlates well to the ~6.6 μm thick topmost layer shown in Figs. 2e&3e. The highest measured hardness value on N450-TWIP is 14.4 GPa at a depth

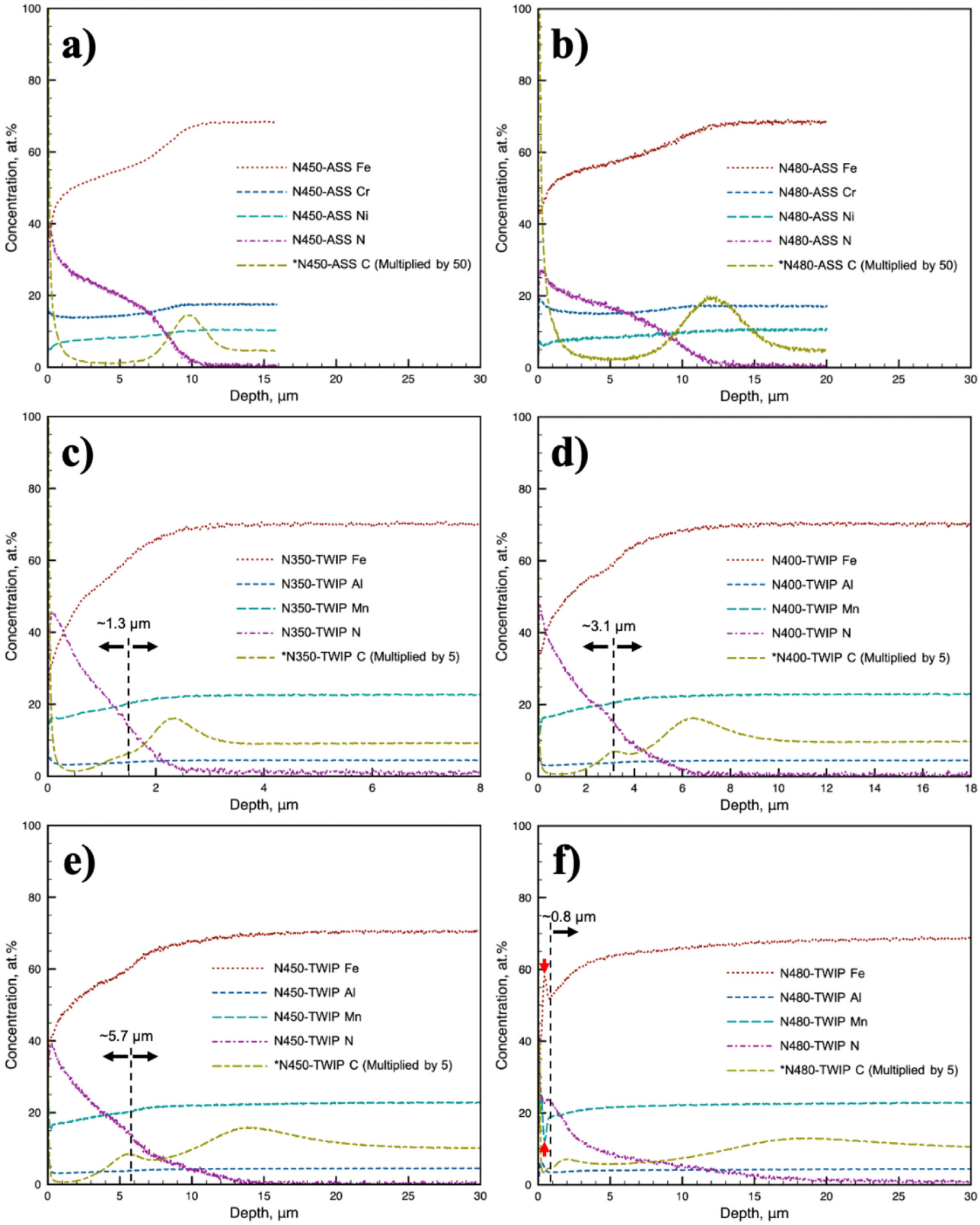

Fig. 3. GDOES composition depth profiles for ASS steel after ASPN at (a) 450 °C and (b) 480 °C, and TWIP steel after ASPN at (c) 350 °C, (d) 400 °C, (e) 450 °C and (f) 480 °C. *Carbon profile is intensified by a factor of 50 for ASS and a factor of 5 for TWIP steel.

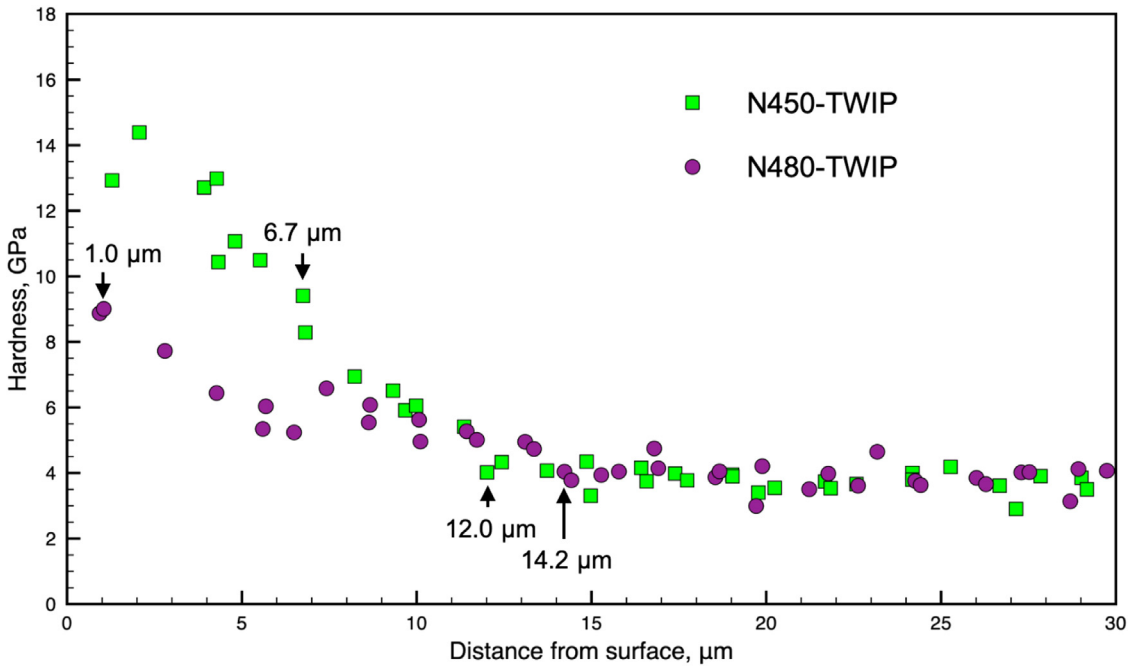

Fig. 4. Nanoindentation hardness-depth profiles for TWIP steel after ASPN at 450 and 480 °C.

of 2.1 μm. The underlying region beyond the depth of 6.7 μm on N450-TWIP shows much lower surface hardness values (below ~9 GPa), which gradually reduce until the unmodified core. Compared with N450-TWIP, N480-TWIP presents with a) reduced hardness values at surface and b) a shallow profile of reducing hardness down to the material core (7.7 GPa at a depth of 2.8 μm to ~4 GPa at a depth of 14.2 μm) in Fig. 4. Noticeably, the highest nanoindentation hardness value for N480-TWIP is 9.0 GPa at a depth of 1.0 μm, which is comparable to the hardness value of 9.4 GPa at a depth of 6.7 μm (i.e. at the start) for the underlying layer on N450-TWIP.

3.4. Surface phase composition

3.4.1. XRD analysis

On N450-ASS, the formation of nitrogen-expanded austenite is evident with the characteristic anisotropic XRD peak shifting (to the left from $\gamma_{substrate}$) in Fig. 5a. This corresponds to an 'aparent' lattice expansion of ~7.2% for the FCC(111) peak, shifting from 43.6 ° to 40.5 °, and ~9.6% for the FCC(200) peak, shifting from ~50.6 ° to ~45.9 °. In contrast, the TWIP steel ASPN-treated at 350–450 °C presented isotropic peak shifting, i.e. ~5.7-5.8% lattice expansion for both FCC(111) and FCC(200) peaks (Fig. 5b). After ~3 μm layer removal, the ground N450-TWIP shows no significant change in peak position (Fig. 5b). Compared to the reference γ'-Fe_4N from powder diffraction (PDF) card 01-071-1297, these 'new' XRD peaks on ASPN-treated TWIP at 350–450 °C are most likely owing to the formation of Fe_4N-type γ' nitride (Fig. 5b).

Due to the Cr-nitride formation and decomposition of γ_N at elevated nitriding treatment temperatures, CrN and α peaks were expected, and found, on N480-ASS in Fig. 5a. The γ_N(111) and γ_N(200) peaks for N480-ASS in Fig. 5a can be attributed to residual γ_N. On the other hand, compared to those treated at 350–450 °C, a substantial microstructure change appears to have developed on 480°C ASPN-treated TWIP steel, as evidenced by the significantly different XRD phase profile of N480-TWIP (Fig. 5b). Given the high chemical affinity between Al and N, AlN precipitation has been anticipated, but no AlN XRD peaks could be identified for N480-TWIP.

Correct identification of the unexpected phases formed on N480-TWIP is important for understanding the 'decomposition' mechanism involved. Considering that the X-ray attenuation depth is > 2 μm on TWIP steel, and a < 1 μm thick topmost layer on N480-TWIP, the XRD profile for N480-TWIP corresponds to both the topmost and the underlying layers. To aid phase identification, N480-TWIP was ground to remove ~3 μm from the surface to remove the topmost layer. Three peaks can be seen on the ground surface at positions slightly left-shifted from $\gamma_{substrate}$ – that can be denoted as $\gamma_{N(i)}$ (see further discussions in Section 4.2) – corresponding to the underlying layer on N480-TWIP. XRD peaks of $\gamma_{N(i)}$ (with < 1% lattice expansion to $\gamma_{substrate}$) can be identified on as-treated N480-TWIP in Fig. 5b, which gradually shift towards $\gamma_{substrate}$ after surface grinding. Similar $\gamma_{N(i)}$ XRD peaks can also be seen on N350-TWIP at the left of the $\gamma_{substrate}$ peaks as indicated in Fig. 5b, owing to X-ray attenuation through the thin (~1.4 μm) topmost layer. The absence of such $\gamma_{N(i)}$ XRD peaks on N400-TWIP and N450-TWIP can be attributed to the thick γ'-Fe_4N layer on those samples.

Most importantly, for N480-TWIP, those peaks other than $\gamma_{N(i)}$ originate from the topmost surface layer. Among these XRD peaks, two peaks at 2θ angles of 44.6 ° and 64.8 ° in Fig. 5b show good match to body-centered cubic (BCC) α-Fe, which should contain N from the nitriding atmosphere and can be denoted as BCC-α_N. The remaining three peaks at 2θ angles of 35.1 °, 40.7 ° and 58.9 ° correspond to an FCC structure with lattice parameter at ~0.44 nm, which corresponds well to a MnO phase (and is further supported by the S/TEM-EDX analysis in Section 3.4.2). Noticeably, the BCC-α_N on N480-TWIP – as further revealed being a continuous surface layer (see TEM characterisation below in Section 3.4.2) – is different from the thin BCC-structured nano-lamellae in cellular decomposion regions in S-phase [30,45].

3.4.2. TEM characterisation

N400-TWIP, N450-TWIP and N480-TWIP were further investigated under TEM. Electron diffraction patterns (EDPs) in Fig. 6b–d (taken at depths < 5 μm) show typical FCC spots with forbidden diffraction reflections for the topmost γ' layer on N450-TWIP.

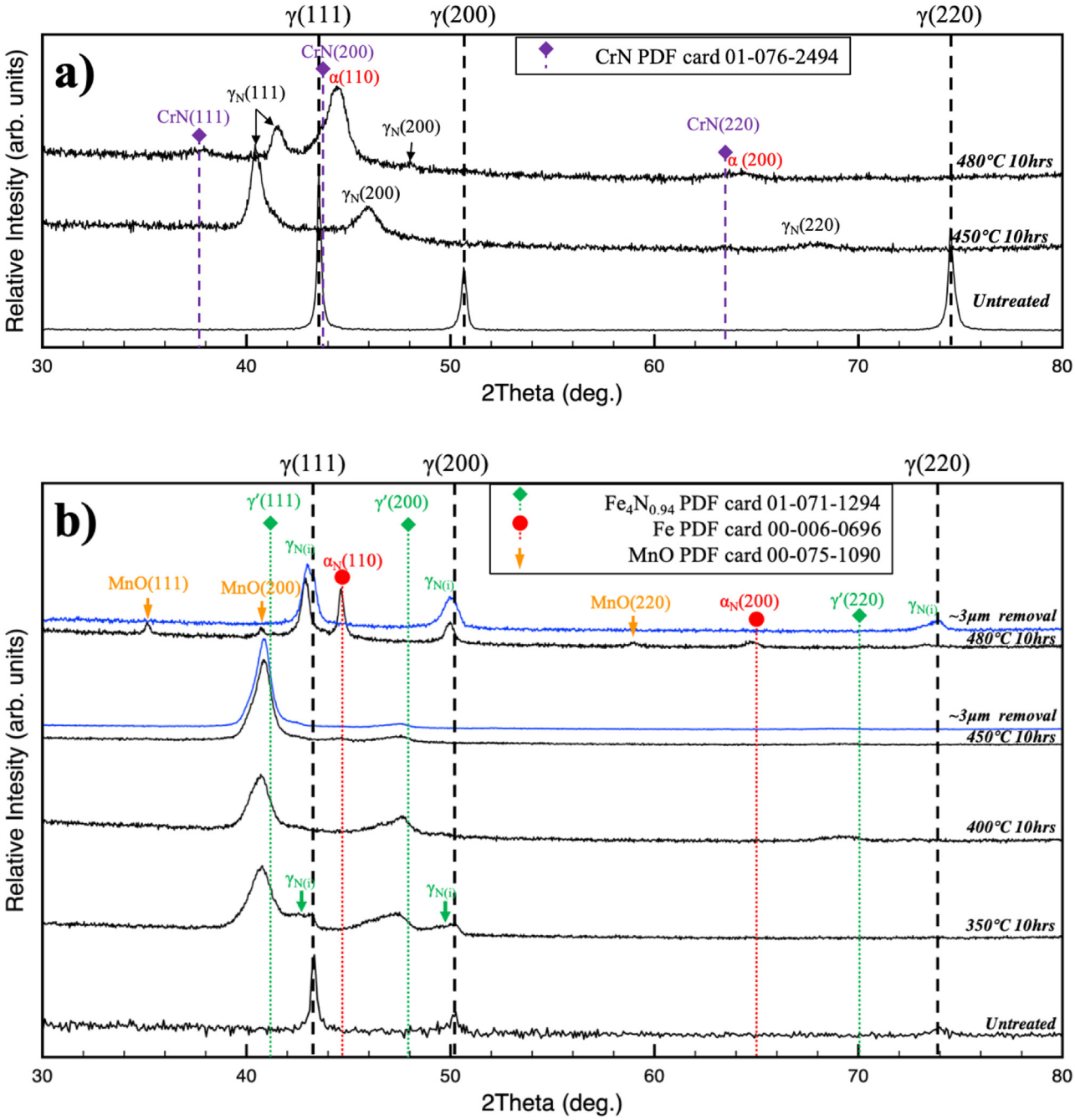

Fig. 5. XRD profiles for (a) AISI 316 ASS and (b) TWIP steel before and after ASPN. Both N450-TWIP and N480-TWIP were ground to remove ~3 μm thick surface layer. The XRD profiles for these ground samples are presented in blue colour in Fig. 5b.

These forbidden FCC reflections (as indicated by arrows in Fig. 6b–d) are attributable to the ordered occupation of N atoms at octahedral interstices, which reaffirm the γ'-Fe_4N type structure. EDPs for the underlying $\gamma_{N(i)}$ layer were taken at a depth of ~5 μm on N400-TWIP, which reveal an FCC structure without forbidden diffraction reflections (Fig. 7b&c), suggesting interstitial solid solution of nitrogen (and carbon, giving its significant C content under GDOES in Fig. 3d).

BF-TEM image in Fig. 8a reveals several phase constituents at the topmost surface of N480-TWIP. STEM-EDX analysis was also carried out to reveal the chemical composition and aid in phase identification on N480-TWIP (Fig. 9). EDX maps of Si and C did not reveal valuable information (owing to the low chemical concentration and the light element nature) and hence are not presented in Fig. 9. Below the Pt deposition layer, a porous "external" region can be seen above the surface (labelled as Region I in Fig. 9). More importantly, using a ~700 nm diameter diffraction aperture, EDP shows polycrystalline rings at the dense "internal" surface on N480-TWIP (below the flat surface line in Fig. 8a and Fig. 9). . A thick ~500–700 nm "internal" region was revealed and labelled as Region II in Fig. 9 (and shown at a lower magnification in Fig. A1, Appendix A). The EDX data in Fig. 9 indicates that Region II is composed of Fe-depleted & Mn/O-rich phase(s) within a low-Mn & Fe-rich matrix, which corresponds to the polycrystal rings seen in Fig. 8b. Hence, the polycrystal rings in EDP (Fig. 8b) and the 'new' surface XRD peaks (Fig. 5b) for N480-TWIP can be indexed as FCC-MnO and BCC-α_N. Considering a nitriding atmosphere and the homogenous N distribution within Region II (Fig. 9f), the MnO

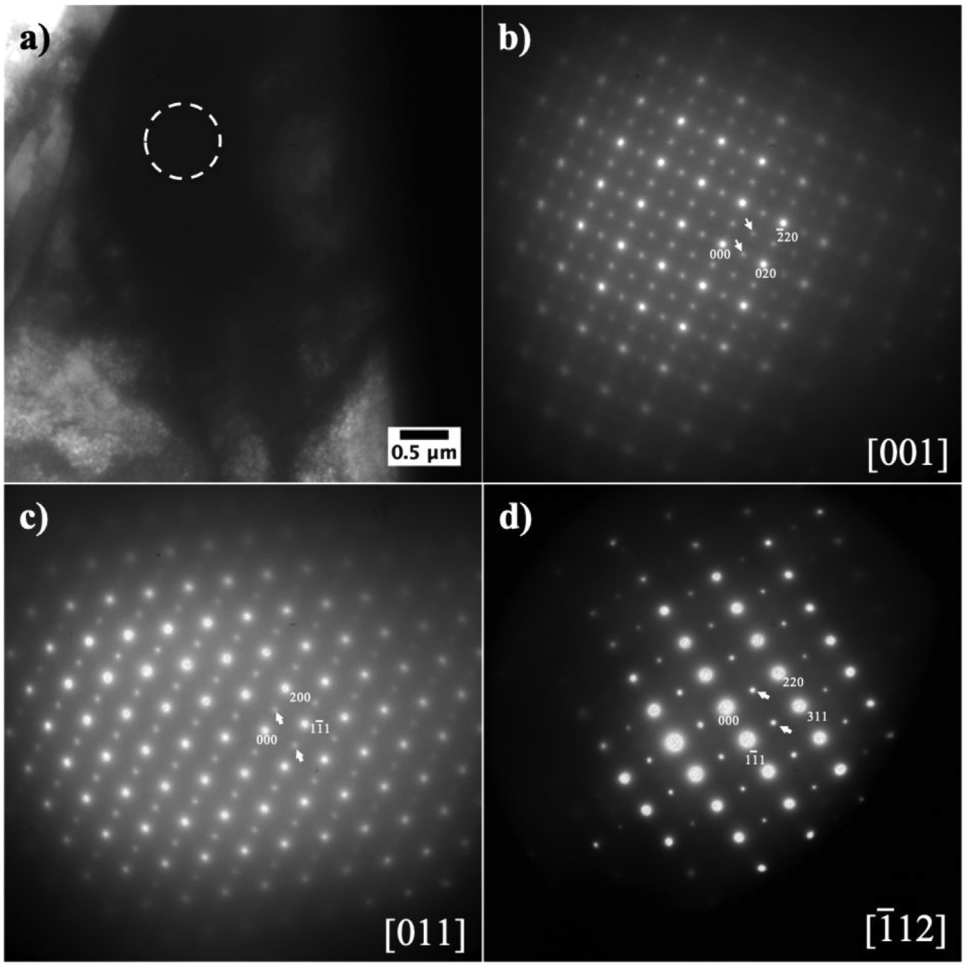

Fig. 6. (a) BF-TEM image and b-d) EDPs for the topmost layer on N450-TWIP (taken at location ~3 μm from the surface). The diffraction aperture position is indicated in Fig. 6a. Forbidden FCC reflections are indicated using arrows.

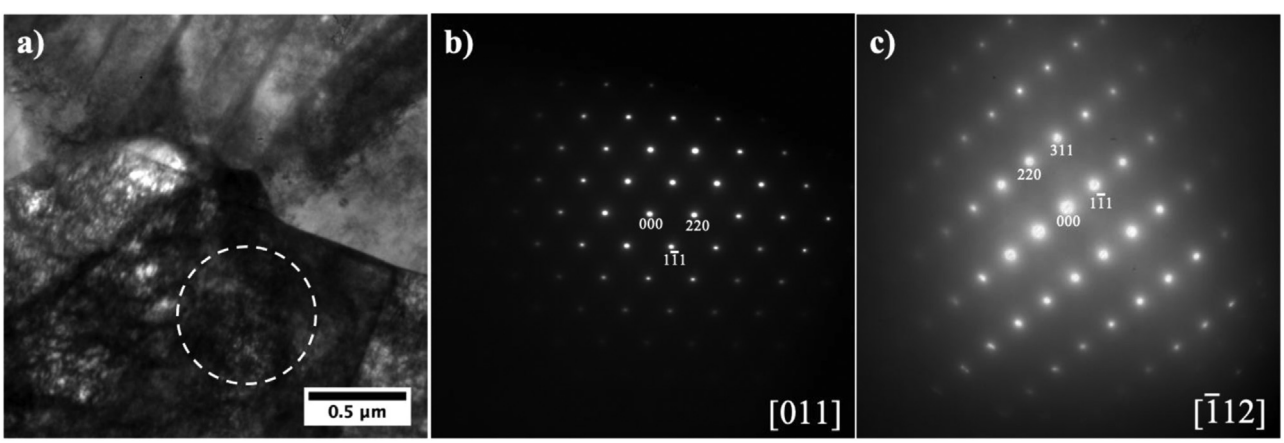

Fig. 7. (a) BF-TEM image and (b), (c) EDPs for the underlying layer on N400-TWIP. Images were taken at depth of ~5 μm from the surface on the cross-sectional TEM sample. The diffraction aperture position is indicated in Fig. 7a.

particles could contain N content (similar to that in α_N) and might be expressed as Mn(O, N).

Apart from Region II, the topmost Region I is composed of nano-structural features above the dashed surface lines (Figs. 8a&9). Since Pt was deposited prior to FIB milling, a dashed line can be drawn based on the Pt contrast in Fig. 9b under STEM-EDX analysis. From surface to core on N480-TWIP, round Fe-nitride nanoparticles of ~50–150 nm in diameter (rich in Fe and N, as demonstrated in Fig. 9a&c&f) – as also found under SEM from the top (Fig. 1b) – were observed directly beneath the Pt deposition, which are attributable to Fe_xN nitride depositions that originate from material transfer from the active screen [37–40]. Mn-oxide bands, as demonstrated in Fig. 9a&d&g, are observed below the Fe_xN nanoparticles. Noticeably, different to the topmost

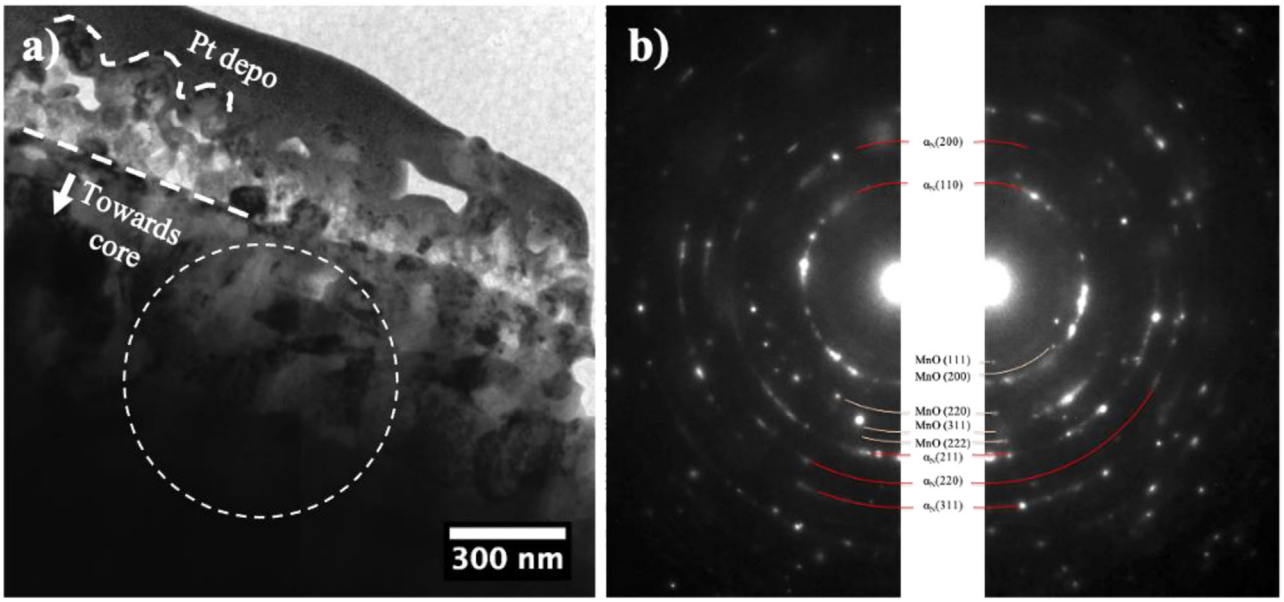

Fig. 8. (a) BF-TEM image and (b) selective area EDP for N480-TWIP surface. The diffraction aperture position is indicated by the dashed circle in Fig. 8a.

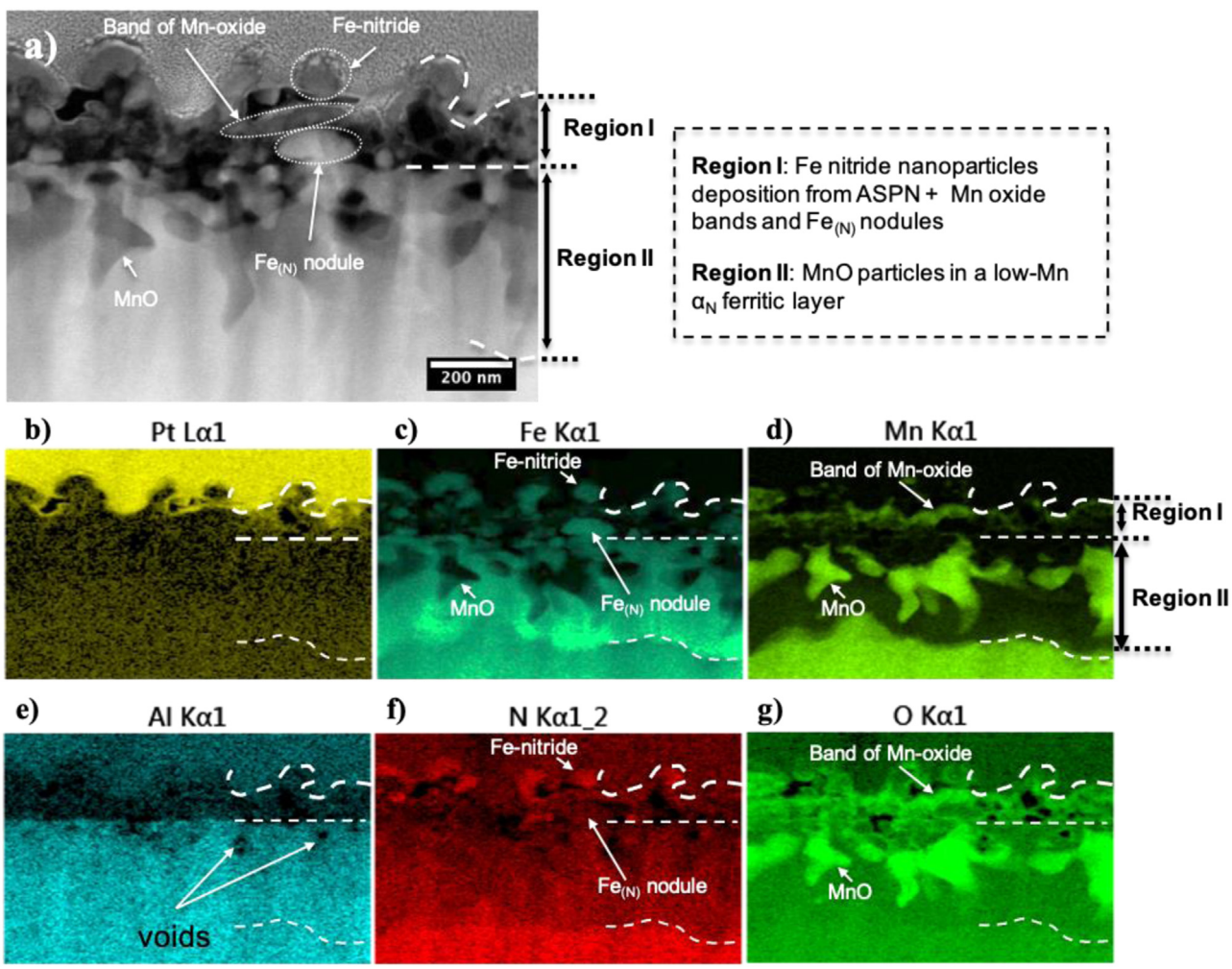

Fig. 9. (a) STEM-HAADF image for the topmost surface of N480-TWIP, and corresponding EDX maps for elements: (b) Pt, (c) Fe, (d) Mn, (e) Al, (f) N, and (g) O, respectively.

Fe_xN nitride nanoparticles, some $Fe_{(N)}$ nodules are observed at the bottom of Region I with much lower N content (see Fig. 9c&f), which are attributed to N-containing BCC-Fe. The flat dashed line drawn in Figs. 8a&9, which marks the interface between Region I and II, were found consistent with the boundary in Al contrast in Fig. 9e. Intriguingly, while no significant elemental segregation was found for Al, outward migration of Mn (and Fe) appears to follow 480°C ASPN (see further discussions on "selective oxidation" in Section 4.3).

4. Discussion

4.1. On the topmost Fe_4N-type layer formed after ASPN at 350–450 °C

Similar topmost layers were obtained on TWIP steel after ASPN at 350–450 °C (Fig. 2c–e), which exhibit a high N content (Fig. 3c–e) and high hardness values (e.g., above ~10 GPa on N450-TWIP in Fig. 4). Different to the anisotropically expanded γ_N-316, these topmost layers on TWIP steel correspond to an isotropic lattice expansion under XRD. The ground N450-TWIP shows no appreciable change in peak position (Fig. 5b). The consistent (or 'unvaried') XRD peak positions for these topmost layers in Fig. 5b (i.e., after ASPN at 350–450 °C, and before/after grinding on N450-TWIP) and the forbidden FCC reflections (Fig. 6b–d) suggest that the topmost layers consist of a Fe_4N-type compound. Compared to the lattice parameter for γ'-Fe_4N at 0.379 nm, the slightly larger lattice parameter of this Fe_4N-type phase at ~0.384 nm (estimated from XRD peak positions) can be associated with the high Al/Mn content (and probably a slightly higher nitrogen absorption) in TWIP steel. Given the TWIP steel chemical composition and the carbon depletion at the topmost surface (as revealed in Fig. 3), this topmost nitride layer could be identified as γ'-$Fe_{2.88}Mn_{0.96}Al_{0.16}N$. Instead of the "$Fe_4N$-containing S phase" reported on Fe-26Mn-3Al-3Cr-0.3C TWIP steel [46], the surface of Fe-24Mn-2Al-0.45C TWIP steel shows Fe_4N-type nitride (without S phase formation) after ASPN treatments between 350 and 450 °C. As demonstrated in the Fe-Cr-Ni system [25,26], the absence of the S phase (or colossal interstitial supersaturation of nitrogen) is attributable to the limited content of the nitride-forming element (~2 wt% Al) for the Fe-Mn-Al-C alloy used in this study.

The formation of this topmost γ'-$Fe_{2.88}Mn_{0.96}Al_{0.16}N$ layer on ASPN-treated TWIP steel is found to be somewhat similar to the γ'-$Fe_{2.6}Ni_{1.4}N$ obtained on a Cr-free Fe-35Ni (wt.%) Invar steel after TPN at 400 °C [25], despite the different nitriding techniques employed. Given the cubic-to-cubic orientation relationship to the underlying FCC matrix, such γ'-type nitride could form from the FCC matrix via interstitial ordering without the migration of substitutional elements at low nitriding treatment temperatures. Noticeably, cellular decomposition regions of low-Ni Fe_4N-type γ' and high-Ni (low-N) γ-Fe lamellae were observed on Fe-35Ni Invar steel after TPN, presumably due to the migration of substitutional elements at elevated temperature of 425–450 °C [25]. However, such cellular decomposition was not seen on ASPN-treated TWIP steel in this study. It appears that the γ'-$Fe_{2.88}Mn_{0.96}Al_{0.16}N$ is thermodynamically more stable than γ'-$Fe_{2.6}Ni_{1.4}N$, which might be associated with the good chemical affinity between Mn and N (compared to that between Ni and N).

4.2. On the underlying interstitial solid solution – $\gamma_{N(i)}$

On ASPN-treated TWIP steel, anisotropic lattice expansion was not observed. However, an underlying N-modified interstitial solid solution is evident after all ASPN treatments at 350–480 °C, which shows a reducing profile towards the core, in both nitrogen concentration (Fig. 3c–f) and hardness (Fig. 4). These underlying N-modified layers present small lattice expansions, as evidenced by (i) the 'shoulder' XRD peaks near $\gamma_{substrate}$ for N350-TWIP and (ii) the XRD profiles for N480-TWIP before/after grinding (Fig. 5b). XRD peaks for this underlying layer on N480-TWIP shift slightly towards $\gamma_{substrate}$ after grinding (Fig. 5b), which suggested different degrees of lattice expansion corresponding to varying levels of nitrogen absorption.

As FCC electron diffraction spots were seen without forbidden reflections in Fig. 7, this layer is considered a disordered interstitial solid solution of nitrogen. Nitrogen-supersaturated layers on AISI 316 ASS possess large lattice expansions with lattice parameters ranging from 0.375 to 0.400 nm at colossal nitrogen absorption levels at ~14–38 at% [8,47]. In contrast, the 'apparent' lattice parameter expanded from 0.362 to 0.365 nm on ASPN-treated TWIP (estimated from the $\gamma_N(111)$ XRD peak positions). Such small lattice expansion is comparable to the previously reported one on Fe-35Ni (wt%) Invar steel following TPN treatments (with 'apparent' lattice parameter between ~0.360 and 0.368 nm) [25].

As proposed in Ref. [25], the slightly-expanded phase on TWIP steel can be denoted as $\gamma_{N(i)}$, being expanded austenite at small interstitial solvency. The colossal interstitial-supersaturated and anisotropically expanded austenite on ASS can be denoted as $\gamma_{N(ii)}$. Moreover, the $\gamma_{N(ii)}$ layers obtained on ASSs are depleted in carbon (as demonstrated in Fig. 3a), which can be attributed to the occupation of "trap site" (formed by the Cr atoms) by N. Nevertheless, GDOES profiles from Fig. 3c–f revealed a significant C content (estimated at levels >1.2 at% C) for the underlying $\gamma_{N(i)}$ layer on TWIP steel. For the carbon hump at the layer/substrate interface, the carbon atoms in $\gamma_{N(i)}$ – or, to be precise, $\gamma_{C,N}$ – also appear to be pushed inward under the accommodation of nitrogen, similar to the phenomena observed for $\gamma_{N(ii)}$. However, the interstitial carbon atoms are only partially displaced by N in $\gamma_{N(i)}$, rather than the complete C-depletion observed for $\gamma_{N(ii)}$. In addition to the differences in nitrogen absorption level and lattice expansion, this carbon solubility in $\gamma_{N(i)}$ signifies another apparent discrepancy between $\gamma_{N(i)}$ and $\gamma_{N(ii)}$.

The maximum equilibrium nitrogen solubility in γ-Fe in the Fe-N binary system is ~10.3 at% N, which would produce estimated lattice parameter at ~0.365 nm [48], using the equation $a = 0.3572 + (0.00078 \times \text{at.\% N})$, a denotes lattice parameter [49]. For $\gamma_{N(ii)}$ on AISI 316 ASS, it has been derived that $a = 0.36395 + (0.05987 \times y_N)$, where y_N denotes the nitrogen occupancy per metal atom [47]. However, so far, there is no such relationship reported between material composition (per unit N absorption) and lattice parameter for $\gamma_{N(i)}$. The lattice parameters of $\gamma_{N(i)}$ from this study and Ref. [48] were estimated from (GA)XRD data, which represented an averaged value, covering volumes from the surface to certain depths (with gradually reducing lattice parameter towards the core). For future investigations, it would be scientifically valuable to establish such a quantitative relationship for $\gamma_{N(i)}$ through the synthesis and examination of 'chemically-homogenous' foil/powder specimens, e.g. under prolonged gaseous nitriding across different nitriding potentials [8].

Additionally, comparing the XRD profiles between untreated TWIP steel and N480-TWIP from Fig. 5b, there is a slight increase in intensity for $\gamma_N(200)$ XRD peak following ASPN at 480 °C. The treatment temperature at 480°C is very low for recrystallisation to occur on TWIP steel [50,51]. The material core showed no signs of recrystallisation. Comparing the XRD profiles for the core/surface of N480-TWIP (see Fig. A2, Appendix A), such an increase in $\gamma_N(200)$ peak intensity originates from the $\gamma_{N(i)}$ layer. Given the crystallographic texture evolution reported in $\gamma_{N(ii)}$ on ASSs [52–55], the increase in $\gamma_{N(i)}(200)$ peak intensity on TWIP steel might

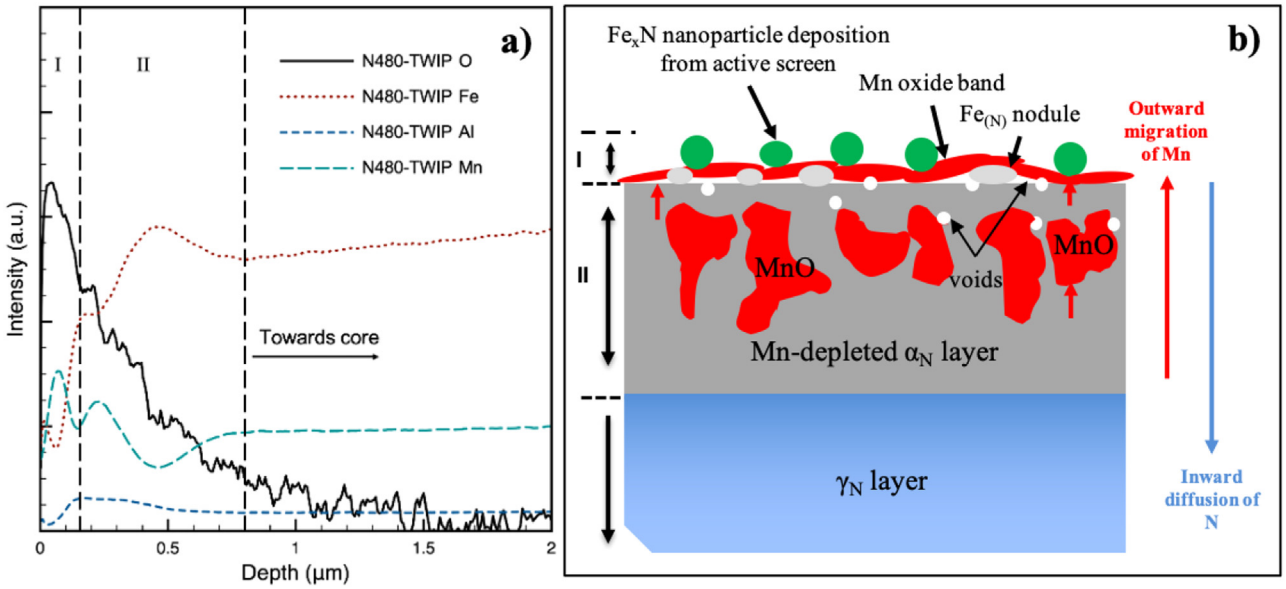

Fig. 10. (a) GDOES composition depth profiles for O, Fe, Al and Mn on N480-TWIP to a depth of 2 μm (note that y-axis is intensity) and (b) schematic illustration for the surface of N480-TWIP to show a synergistic selective oxidation mechanism during ASPN.

be associated with lattice rotation under nitrogen-induced (compressive) strain, which points to systematic EBSD studies in future explorations.

4.3. Selective oxidation on TWIP steel during ASPN

In agreement with the change in layer morphology and the reduction in surface hardness, N480-TWIP showed a unique surface microstructure, that was substantially different from those obtained at 350–450 °C. A nitride precipitation-induced decomposition mechanism was anticipated (similar to the CrN precipitation in high-Cr ASSs after nitriding); however, no signs of AlN formation were observed. Both XRD (Fig. 5b) and TEM analysis (Figs. 8 and 9) indicated MnO formation on N480-TWIP. Within the ~0.7–0.8 μm thick topmost layer on N480-TWIP, two surface regions can be identified (as schematically illustrated in Fig. 10b):(a) Region I: an ~100–300 nm thick "external" zone, and (b) Region II: a ~500–700 nm thick MnO-containing α_N-Fe layer. The "external" MnO bands in Region I and the distribution of MnO particles in (the upper region of) Region II correlate well to the fluctuations in the composition-depth profiles in Fig. 10a. The surface microstructure on N480-TWIP strongly associates with Mn-oxide formation.

4.3.1. On outward elemental migration

The elevated treatment temperature played a decisive role in MnO formation, considering the change in surface microstructure only at 480 °C, across a treatment temperature range of 350–480 °C. Above a threshold ASPN treatment temperature between 450 and 480 °C, a selective oxidation mechanism (via reaction: $Mn + \frac{1}{2}O_2(g) \rightarrow MnO$) occured at the topmost surface and outcompeted nitridation (for forming γ'-Fe_4N, which predominated at $\leq$ 450°C). Thermally-activated outward elemental migration seems a plausible explanation for the "layered" phase distribution on N480-TWIP (Fig. 10b).

Firstly, the unique phase composition and distribution in the "external" Region I – i.e., from top to bottom, Fe_xN nitride nanoparticles, Mn-oxide bands and $Fe_{(N)}$ nodules (as revealed in Section 3.4.2 and illustrated in Fig. 10b) – suggest outward elemental migration, in comparison to a (sputtering-)deposition mechanism. Apart from the topmost Fe_xN nanoparticles – which could originate from ion sputtering from the active screen (i.e., as demonstrated in [37–40]) – the ~100–150 nm thick "external region" of Mn-oxide bands and $Fe_{(N)}$ nodules on N480-TWIP has never been previously observed after ASPN treatments [36–40,56]. The Mn-oxide bands in Region I (Fig. 10b) cannot be attributed to material transfer from the active screen, as the stainless-steel active screen contains low Mn content (i.e., < 2 wt%).

Consider an extreme scenario where a significant amount of metal atoms was sputtered from the sample and deposited back, the "external" region would be composed of a "blend" of phases under deposition. This is inconsistent with the layered phase distribution observed for Region I. Moreover, if Fe atoms were sputtered and deposited onto the sample surface during ASPN, the deposition products should be Fe_xN nitride nanoparticles produced within the nitriding atmosphere. The $Fe_{(N)}$ nodules at the bottom of Region I cannot be attributed to a (sputtering-)deposition mechanism.

Rather than being deposited, the Mn-oxide bands and $Fe_{(N)}$ nodules in Region I (Fig. 10b) appear to grow from the surface, which is attributable to outward migration of Mn (and Fe) under oxidation reaction. The typical phase composition and distribution on N480-TWIP (i.e. "external" Mn-oxide bands and $Fe_{(N)}$ nodules in Region I, and an underlying MnO-containing ferritic layer in Region II) is found analogous to the oxidised surfaces formed on Fe-Mn-Si [57] and high-Mn TWIP steels [58–60] after thermal annealing in $N_2 + H_2$ atmosphere before the hot-dip galvanising process. Compared to the severely oxidised high-Mn steels after annealing at 600–800 °C [57–60], the thin nano-structure on N480-TWIP can be attributed to early-stage oxidation at a lower temperature of 480 °C. The "external" Mn-oxide bands (with thickness ranging between ~30 and 60 nm) in Region I on N480-TWIP (Fig. 10b) can be compared with the thick continuous "external" MnO mono-layer (with thickness ranging between ~200–500 nm at 600–800 °C) from Ref. [58–60]. Similar to the ~30–120 nm $Fe_{(N)}$ nodules in Region I on N480-TWIP (Fig. 10b), "protruded ferrite grains" and "overflowing" Fe particles were reported on TWIP [60] and TRIP steel [61] after thermal annealing, which was attributed to the outward migration of Fe under the volume expansion of internal oxide formation [61,62].

4.3.2. On oxygen partial pressure and substrate chemical composition

Selective oxidation of Mn on TWIP steel also requires oxygen content in the processing chamber. For ASPN in this study, the base

pressure is < 0.01 mbar (see Experimental) and the vacuum chamber is continuously evacuated by vacuum pumps. In opposite to oxidation, surface iron oxides on steels can be nitrided following ASPN treatments in the reducing atmosphere of $H_2 + N_2$ gas mixtures (i.e., oxides on a pre-oxidised 3% Cr low-C 722M24 steel, after ASPN at 500 °C [63,64]). The low oxygen partial pressure was often neglected for plasma nitriding of steels. In this case, the occurrence of selective oxidation on TWIP steel is associated with the unconventional high-Mn substrate, which appears to be sensitive to the oxygen content in the treatment atmosphere.

Furthermore, MnO formation is consistent with the low oxygen partial pressure during ASPN. Amongst Mn-oxides (i.e., MnO, MnO_2, Mn_2O_3, Mn_3O_4), MnO formation favours low oxygen partial pressure and high temperature [65,66]. The upper oxygen partial pressures (at the phase boundaries) at 480 °C are of the order of 10^{-16} mbar, ~0.06 mbar and ~10^3 mbar for MnO, Mn_3O_4 and Mn_2O_3, respectively [65]. MnO was reported on FeMnSi steels following thermal annealing at 700 °C at oxygen partial pressure as low as 2.9×10^{-20} mbar [57]. Thermo-calc® simulation was carried out for the oxide formation with respect to oxygen partial pressure on a Fe-24Mn-2Al-0.45C TWIP steel composition at 480 °C, which unambiguously revealed that Halite (MnO/FeO) is the predominant phase at the lowest oxygen partial pressures (Fig. A3, Appendix A). Nevertheless, further thermodynamic modelling studies on the reaction kinetics and phase stability will be beneficial, which needs to take into account the competition between oxidation and nitridation for the different elements from the TWIP steel substrate in a low-pressure nitriding atmosphere. Noticeably, the ΔG°_f values cannot be used to explain the preferential phase formation during ASPN. For example, although the standard Gibbs free energy of formation (ΔG°_f) for Fe_3O_4 at -1250 kJ.mol^{-1} (at 480 °C [67]) is significantly lower than that for MnO at -330 kJ.mol^{-1} (between 427 and 527 °C [68]), MnO formed with no signs of Fe_3O_4 on N480-TWIP.

In addition, both high Al and Si substrate contents (or Al/Mn and Si/Mn ratios) could influence oxide formation on FeMnAlSiC TWIP steels. At high Al/Mn ratios, Al_2O_3 formation is preferred over MnO on FeMnAlC steels under thermal annealing in $H_2 + N_2$ gas mixtures [69]. The thermodynamic study by Zhang et al. [57] also suggests that MnO is not expected on FeMnSi alloys with high Si contents. Moreover, after gaseous nitriding at 500/550 °C, AlN was reported (with no signs of Mn-oxide formation) on high-Al FeMnAlC steels (i.e., Fe-28Mn-9Al-1.8C [70], Fe-30Mn-9Al-1.8C [71], and Fe-30Mn-10Al-1C [72]). A high Al (or Si) content in TWIP steel substrate seems to promote nitridation reaction during nitriding, which could prevent selective oxidation of Mn.

4.3.3. The synergistic selective oxidation during nitriding and implications

The selective oxidation mechanism has pronounced influences on the N absorption of TWIP steel during ASPN treatment. Firstly, a porous nanostructured topmost Region I (Fig. 10b) formed during ASPN that allowed simultaneous N inward diffusion in nitriding treatment conditions, compared to the extreme case of a dense oxide layer that can block N inward diffusion. Secondly, MnO formation led to Mn-depletion in the surrounding matrix, which destabilised the austenitic phase and formed a continuous BCC-structured ferritic layer (Region II, Fig. 10b). The nanocrystalline structure of the ferritic layer (noting the electron diffraction rings in Fig. 8b) provides increased defect density for interstitial inward diffusion.

Moreover, the continuous low-Mn α_N layer most likely possesses a low N solubility, which can effectively reduce surface N concentration and limit N absorption in the underlying region. Noticeably, both the "flattened" N profile at depth < 0.8 μm (under GDOES, Fig. 3f) and the low N contrast (under STEM-EDX, Fig. 9f) for Region II on N480-TWIP suggest a rather low N content. The N level at ~21–22 at% N (from GDOES, Fig. 3f) is apparently too high for a BCC-structured α_N-Fe layer and could be interfered with by its neighbouring high-N features, such as the topmost Fe_xN depositions. The depth-profiling GDOES analysis did not yield reliable chemical compositions for this thin surface layer, given technical limitations such as (i) non-uniform sputtering (owing to surface roughness, grain orientation and phase composition/distribution) and (ii) size/depth variations for features across a large sampling area (i.e., 2.5 mm diameter sputtering crater).

Most importantly, under the synergetic action of selective oxidation and nitrogen inward diffusion, a thick diffusion zone was eventually achieved on high-Mn TWIP steel without a compound layer. Although such an oxidation mechanism reduces the total surface nitrogen uptake during nitriding treatments, the thick compound-free diffusion layer obtained could be advantageous for tribological applications. Considering the necessities discussed for MnO formation in Sections 4.3.1 and 4.3.2, synergistic selective oxidation could occur on a wide range of TWIP steels under different thermochemical diffusion treatments at different oxygen partial pressures (i.e., not restricted to Fe-24Mn-2Al-0.45C steel and ASPN technology). The selective oxidation of steels has been frequently visited owing to its adverse effect on surface wettability to molten zinc during galvanising processes [57,58,61,73–76]. Nevertheless, the synergistic action revealed between selective oxidation and N absorption in this study potentially provides a new surface engineering strategy of 'oxy-'nitriding for high-Mn TWIP (or TRIP) steels. Different to 'conventional' oxy-nitriding, the selective oxidation mechanism could be exploited to control N uptake of TWIP steel *in-situ* during 'oxy-'nitriding treatment.

Comparing the surface of N480-TWIP at 480 °C and those after thermal annealing at 600–800 °C [57–60], more severe oxidation can occur on TWIP steel at higher nitriding temperatures. Both the substrate chemical composition and the level of oxygen partial pressure in treatment atmosphere can influence oxidation/nitridation reactions and make pronounced impacts on surface microstructure/property. However, there is so far no other experimental data on selective oxidation of high-Mn steels under thermochemical diffusion treatments. This points to future studies on thermochemical diffusion treatments of high-Mn steels with the consideration of alloy chemical composition, treatment temperature and gas composition (typically, the oxygen partial pressure), which will assist in i) predicting (promoting and/or avoiding) selective oxidation and ii) the selection/design of Fe-Mn-Al-Si-C TWIP steels and their surface treatments.

5. Conclusions

This study investigates a Fe-24Mn-2Al-0.45C TWIP steel after ASPN treatments at 350–480 °C, and compared to a Fe-18Cr-11Ni-3Mo AISI 316 ASS that was treated at 450 and 480 °C. Conclusions can be drawn as follows:

- TWIP steel showed isotropic XRD peak shifts after ASPN at 350–450 °C, corresponding to the formation of Fe_4N-type γ'-$Fe_{2.88}Mn_{0.96}Al_{0.16}N$ at the topmost surface. The underlying N-modified layer after ASPN at 350–480 °C is revealed as being an interstitial solid solution of nitrogen (and carbon), that can still be named expanded austenite and denoted as $\gamma_{N(i)}$.
- Compared to the expanded austenite of $\gamma_{N(ii)}$ obtained on ASSs under colossal interstitial absorption, the $\gamma_{N(i)}$ layers obtained on TWIP steel show small lattice expansion with comparatively low N absorption levels and rather high carbon solvency. Upon low-temperature nitriding, the formation of a 'less-expanded'

$\gamma_{N(i)}$ can be associated with the low level of nitride-forming elements in the substrate.

- At an elevated temperature of 480 °C, an unusual nanostructured topmost layer was obtained on TWIP steel, that is composed of a) a ~100–150 nm thick "external" region with MnO bands and $Fe_{(N)}$ nodules and b) a ~700 nm thick MnO-containing α_N layer. The selective oxidation on TWIP steel during ASPN is attributable to (a) an elevated treatment temperature that allowed Mn segregation, (b) a low oxygen partial pressure in the processing atmosphere, and (c) a high-Mn TWIP steel substrate with low Si/Mn or Al/Mn ratio.
- After ASPN at 450 °C, TWIP steel shows significant surface hardening from 310 $HV_{0.025}$ to 1275 $HV_{0.025}$. While the γ' layer on N450-TWIP presents high nanoindentation hardness values above ~10 GPa, the $\gamma_{N(i)}$ layers on both N450-TWIP and N480-TWIP present hardness values below ~8–9 GPa and a gradually reducing hardness profile towards the core. Without a topmost γ' layer, N480-TWIP presents with an average surface hardness value of 738 $HV_{0.025}$, which (although lower than that obtained on N450-TWIP) is still more than double the hardness of untreated TWIP.
- The MnO-induced microstructural evolution at the topmost surface altered the overall N uptake of TWIP steel during ASPN, which led to different surface microstructure and properties. The synergistic action between selective oxidation and N inward diffusion provides insights and potentially points to a new strategy for thermochemical diffusion treatment of TWIP steels.

Declaration of Competing Interest

The authors declare that they have no known competing financial interests or personal relationships that could have appeared to influence the work reported in this paper.

Acknowledgments

We acknowledge the Center for Electron Microscopy in the University of Birmingham for the training/support on the electron microscopes and Dr. Mingwen Bai from Coventry University for the Thermo-Calc® calculation. One of the authors, T.J.C., would also like to thank the studentship from the Center for Doctoral Training in Innovative Metal Processing (IMPaCT) funded by EPSRC, UK (EP/F006926/1).

Appendix A

Figs. A1, A2 and A3.

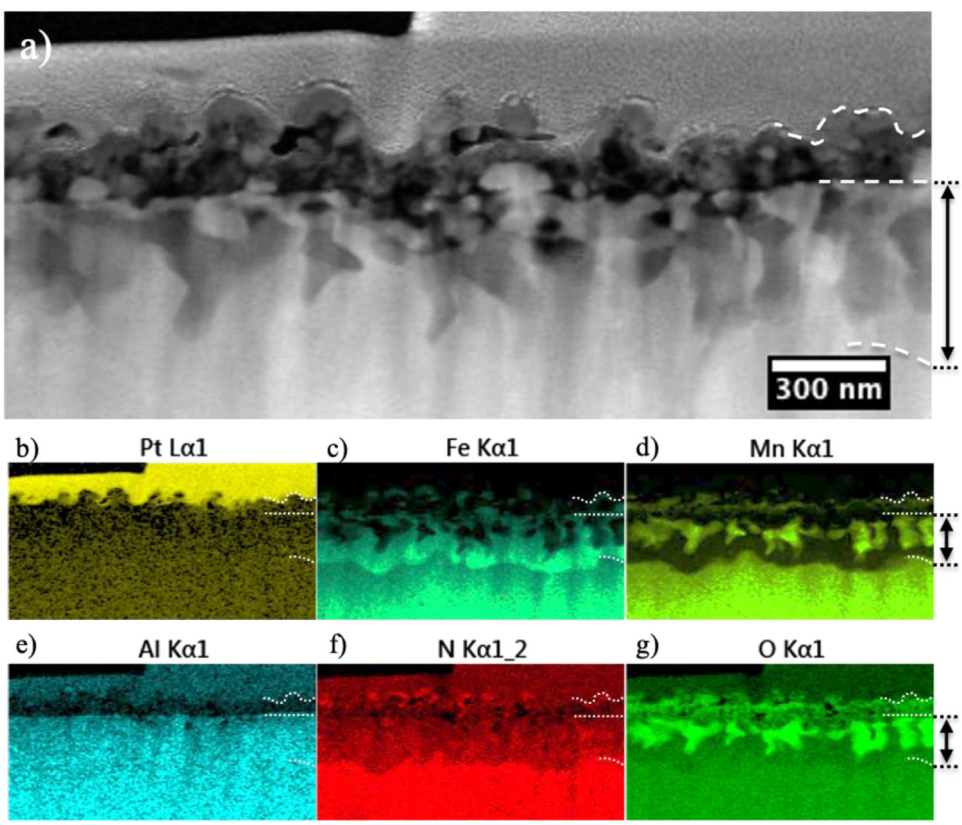

Fig. A1. STEM-EDX analysis at a smaller magnification for an overview of N480-TWIP surface: (a) STEM-HAADF image and corresponding EDX maps for (b) Pt, (c) Fe, (d) Mn, (e) Al, (f) N and (g) O, respectively.

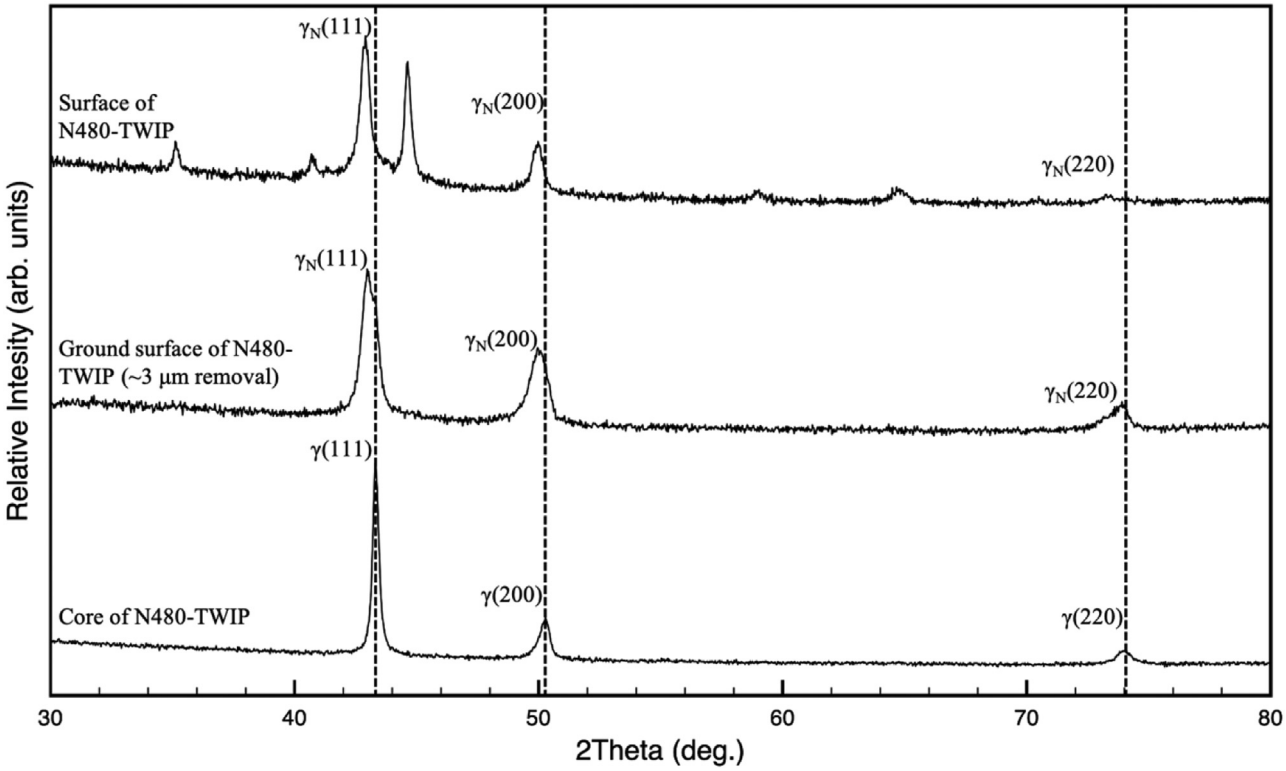

Fig. A2. XRD profiles (from bottom to top) for the core, the ground surface and the surface of the N480-TWIP sample, showing the slight increase in $\gamma_N(200)$ peak intensity for the $\gamma_{N(i)}$ layer.

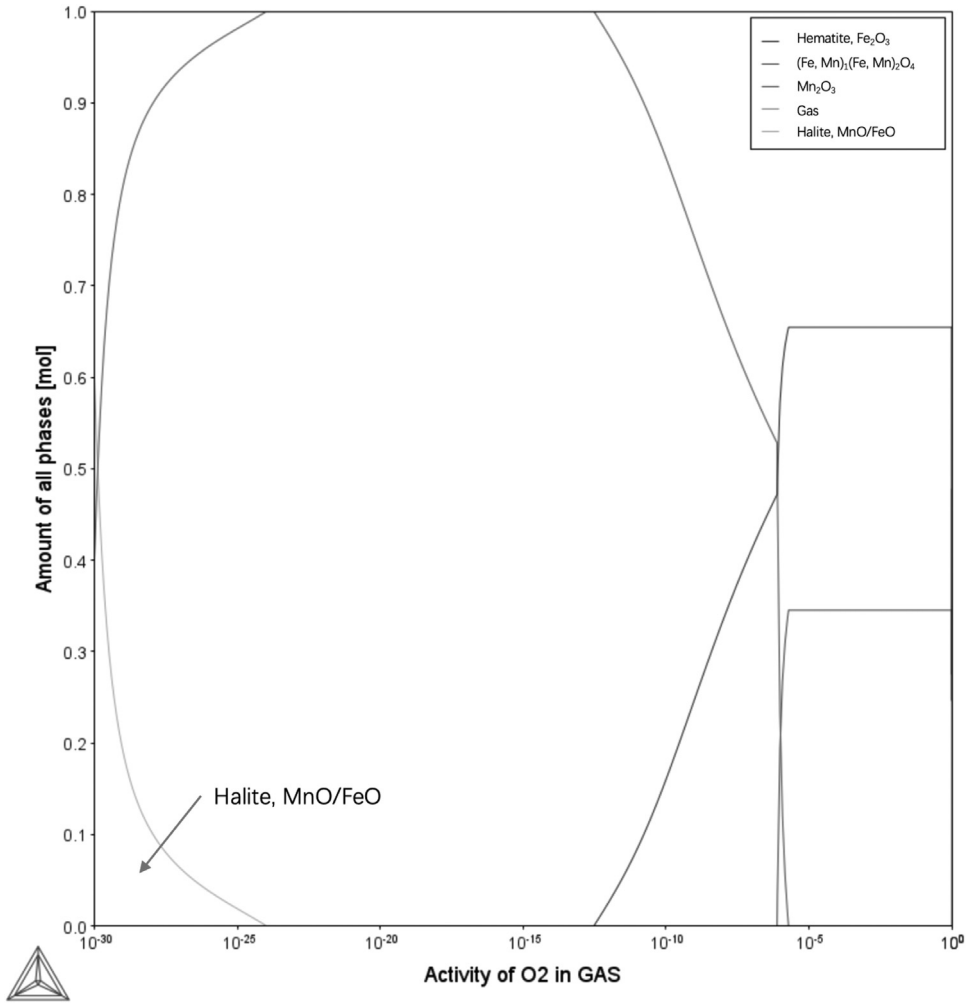

Fig. A3. Thermo-Calc® calculation (Thermo-Calc® 2016b software, TCFe7 database) of oxide formation on Fe-24Mn-2Al-0.45C TWIP steel as a dependency of oxygen activity at 480 °C, showing the Halite (MnO/FeO) formation at the lowest oxygen partial pressure.

References

[1] Z.L. Zhang, T. Bell, Structure and corrosion resistance of plasma nitrided stainless steel, Surf. Eng. 1 (2) (1985) 131–136.
[2] D.L. Williamson, L. Wang, R. Wei, P.J. Wilbur, Solid solution strengthening of stainless steel surface layers by rapid, high dose, elevated temperature nitrogen ion implantation, Mater. Lett. 9 (1990) 302–308.
[3] C.X. Li, T. Bell, Corrosion properties of active screen plasma nitrided 316 austenitic stainless steel, Corros. Sci. 46 (2004) 1527–1547.
[4] C.X. Li, T. Bell, Sliding wear properties of active screen plasma nitrided 316 austenitic stainless steel, Wear 256 (11) (2004) 1144–1152.
[5] D.L. Williamson, O. Ozturk, Metastable phase formation and enhanced diffusion in f.c.c. alloys under high dose, high flux nitrogen implantation at high and low ion energies, Surf. Coat. Technol. 65 (1994) 15–23.
[6] Y. Cao, F. Ernst, G.M. Michal, Colossal carbon supersaturation in austenitic stainless steels carburized at low temperature, Acta Mater. 51 (2003) 4171–4181.
[7] S. Collins, P. Williams, Low-temperature colossal supersaturation, Adv. Mater. Process (2006) 32–33 ASM International.
[8] T. Christiansen, M.A.J. Somers, Controlled dissolution of colossal quantities of nitrogen in stainless steel, Metall. Mater. Trans. A 37A (2006) 675–682.
[9] K. Ichii, K. Fujimura, T. Takase, Structure of the ion-nitrided layer of 18-8 stainless steel, Technol. Rep. Kansai Univ. 27 (1986) 135–144.
[10] S.P. Hannula, O. Nenonen, J.P. Hirvonen, Surface structure and properties of ion-nitrided austenitic stainless steels, Thin Solid Films 181 (1989) 343–350.
[11] A. Leyland, D.B. Lewis, P.R. Stevenson, A. Matthews, Low temperature plasma diffusion treatment of stainless steels for improved wear resistance, Surf. Coat. Technol. 62 (1993) 608–617.
[12] Y. Sun, X.Y. Li, T. Bell, X-ray diffraction characterisation of low temperature plasma nitrided austenitic stainless steels, J. Mater. Sci. 34 (1999) 4793–4802.
[13] T. Christiansen, M.A.J. Somers, On the crystallographic structure of S-phase, Scr. Mater. 50 (2004) 35–37.
[14] B.K. Brink, K. Stahl, T.L. Christiansen, J. Oddershede, G. Winther, M.A.J. Somers, On the elusive crystal structure of expanded austenite, Scr. Mater. 131 (2017) 59–62.
[15] F. Borgioli, From austenitic stainless steel to expanded austenite-s phase: formation, characteristics and properties of an elusive metastable phase, Metals 10 (2) (2020).
[16] D.L. Williamson, J.A. Davis, P.J. Wilbur, Effect of austenitic stainless steel composition on low-energy, high-flux nitrogen ion beam processing, Surf. Coat. Technol. 103-104 (1998) 178–184.
[17] J.P. Riviere, M. Cahoreau, P. Meheust, Chemical bonding of nitrogen in low energy high flux implanted austenitic stainless steel, J. Appl. Phys. 91 (10) (2002) 6361–6366.
[18] H. Dong, S-phase surface engineering of Fe-Cr, Co-Cr and Ni-Cr alloys, Int. Mater. Rev. 55 (2) (2010) 65–98.
[19] F. Ernst, Y. Cao, G.M. Michal, A.H. Heuer, Carbide precipitation in austenitic stainless steel carburized at low temperature, Acta Mater. 55 (2007) 1895–1906.
[20] J. Oddershede, T.L. Christiansen, K. Stahl, M.A.J. Somers, Extended X-ray absorption fine structure investigation of nitrogen stabilized expanded austenite, Scr. Mater. 62 (2010) 290–293.
[21] A. Martinavičius, G. Abrasonis, A.C. Scheinost, R. Danoix, F. Danoix, J.C. Stinville, G. Talut, C. Templier, O. Liedke, S. Gemming, W. Möller, Nitrogen interstitial diffusion induced decomposition in AISI 304L austenitic stainless steel, Acta Mater. 60 (10) (2012) 4065–4076.
[22] A. Martinavičius, R. Danoix, M. Drouet, C. Templier, B. Hannoyer, F. Danoix, Atom probe tomography characterization of nitrogen induced decomposition in low temperature plasma nitrided 304L austenitic stainless steel, Mater. Lett. 139 (2015) 153–156.
[23] K.N. Sasidhar, S.R. Meka, Spinodal decomposition during isothermal gas-solid equilibration – Its effects and implications, Acta Mater. 161 (2018) 266–272.
[24] K.N. Sasidhar, S.R. Meka, Thermodynamic reasoning for colossal N supersaturation in austenitic and ferritic stainless steels during low-temperature nitridation, Sci. Rep. 9 (1) (2019) 7996.
[25] X. Tao, A. Matthews, A. Leyland, On the nitrogen-induced lattice expansion of a non-stainless austenitic steel, invar 36®, under triode plasma nitriding, Metall. Mater. Trans. A 51 (1) (2020) 436–447.
[26] H.L. Che, S. Tong, K.S. Wang, M.K. Lei, M.A.J. Somers, Co-existence of γ'N phase and γN phase on nitrided austenitic Fe-Cr-Ni alloys – I. experiment, Acta Mater. 177 (2019) 35–45.
[27] B.C.D. Cooman, Y. Estrin, S.K. Kim, Twinning-induced plasticity (TWIP) steels, Acta Mater. 142 (2018) 283–362.
[28] J. Buhagiar, X. Li, H. Dong, Formation and microstructural characterisation of S-phase layers in Ni-free austenitic stainless steels by low-temperature plasma surface alloying, Surf. Coat. Technol. 204 (3) (2009) 330–335.
[29] G. Maistro, S.A. Pérez-García, M. Norell, L. Nyborg, Y. Cao, Thermal decomposition of N-expanded austenite in 304L and 904L steels, Surf. Eng. 33 (4) (2017) 319–326.
[30] X. Tao, X. Liu, A. Matthews, A. Leyland, The influence of stacking fault energy on plasticity mechanisms in triode-plasma nitrided austenitic stainless steels: Implications for the structure and stability of nitrogen-expanded austenite, Acta Mater. 164 (2019) 60–75.
[31] X. Tao, J. Qi, M. Rainforth, A. Matthews, A. Leyland, On the interstitial induced lattice inhomogeneities in nitrogen-expanded austenite, Scr. Mater. 185 (2020) 146–151.
[32] X. Tao, X. Li, H. Dong, A. Matthews, A. Leyland, Evaluation of the sliding wear and corrosion performance of triode-plasma nitrided Fe-17Cr-20Mn-0.5N high--manganese and Fe-19Cr-35Ni-1.2Si high-nickel austenitic stainless steels, Surf. Coat. Technol. 409 (2021) 126890.
[33] G. Frommeyer, U. Brüx, Microstructures and mechanical properties of high--strength Fe-Mn-Al-C light-weight TRIPLEX steels, Steel Res. Int. 77 (9-10) (2006) 627–633.
[34] S. Chen, R. Rana, A. Haldar, R.K. Ray, Current state of Fe-Mn-Al-C low density steels, Prog. Mater Sci. 89 (2017) 345–391.
[35] S.C. Gallo, H. Dong, Study of active screen plasma processing conditions for carburising and nitriding austenitic stainless steel, Surf. Coat. Technol. 203 (24) (2009) 3669–3675.
[36] C.X. Li, J. Georges, X.Y. Li, Active screen plasma nitriding of austenitic stainless steel, Surf. Eng. 18 (6) (2002) 453–457.
[37] C.X. Li, T. Bell, H. Dong, A study of active screen plasma nitriding, Surf. Eng. 18 (3) (2002) 174–181.
[38] C. Zhao, C.X. Li, H. Dong, T. Bell, Study on the active screen plasma nitriding and its nitriding mechanism, Surf. Coat. Technol. 201 (6) (2006) 2320–2325.
[39] S.C. Gallo, H. Dong, On the fundamental mechanisms of active screen plasma nitriding, Vacuum 84 (2) (2009) 321–325.
[40] K. Lin, X. Li, H. Dong, P. Guo, D. Gu, Nitrogen mass transfer and surface layer formation during the active screen plasma nitriding of austenitic stainless steels, Vacuum 148 (2018) 224–229.
[41] K. Lin, X. Li, L. Tian, H. Dong, Active screen plasma surface co-alloying treatments of 316 stainless steel with nitrogen and silver for fuel cell bipolar plates, Surf. Coat. Technol. 283 (2015) 122–128.
[42] K. Lin, X. Li, L. Tian, H. Dong, Active screen plasma surface co-alloying of 316 austenitic stainless steel with both nitrogen and niobium for the application of bipolar plates in proton exchange membrane fuel cells, Int. J. Hydrog. Energy 40 (32) (2015) 10281–10292.
[43] K. Lin, X. Li, H. Dong, S. Du, Y. Lu, X. Ji, D. Gu, Surface modification of 316 stainless steel with platinum for the application of bipolar plates in high performance proton exchange membrane fuel cells, Int. J. Hydrog. Energy 42 (4) (2017) 2338–2348.
[44] B. Dashtbozorg, X. Tao, H. Dong, Active-screen plasma surface multi-functionalisation of biopolymers and carbon-based materials – an overview, Surf. Coat. Technol. 442 (2022) 128188.
[45] X.Y. Li, Y. Sun, T. Bell, K. Akamatsu, Transmission electron microscopy study of S phase in low temperature plasma nitrided 316 stainless steel, in: Stainless Steel 2000: Thermochemical Surface Engineering of Stainless Steel, Maney Publishing, London, 2001, pp. 215–228.
[46] X. Yuan, Y. Zhao, X. Li, L. Chen, Effects of gas nitriding temperature on the surface properties of a high manganese TWIP steel, Metals 7 (3) (2017).
[47] T. Christiansen, T.S. Hummelshoj, M.A.J. Somers, Expanded austenite, crystallography and residual stress, Surf. Eng. 26 (4) (2010) 242–247.
[48] H.A. Wriedt, N.A. Gocen, R.H. Nafziger, The Fe-N (iron-nitrogen) system, Bull. Alloy Ph. Diagr. 8 (4) (1987) 355–377.
[49] D.H. Jack, K.H. Jack, Invited review: Carbides and nitrides in steel, Mater. Sci. Eng. 11 (1973) 1–27.
[50] S. Kang, Y.S. Jung, J.H. Jun, Y.K. Lee, Effects of recrystallization annealing temperature on carbide precipitation, microstructure, and mechanical properties in Fe–18Mn–0.6C–1.5Al TWIP steel, Mater. Sci. Eng. A 527 (3) (2010) 745–751.
[51] H. Xue, H. Yuan, K. Guo, Z. Zhang, M. Zhang, Microstructure evolution and recrystallization temperature change of cold-rolled Fe–19Mn–0.6C twinning-induced plasticity steel during annealing, Metals 11 (8) (2021) 1181.
[52] J.C. Stinville, P. Villechaise, C. Templier, J.P. Riviere, M. Drouet, Lattice rotation induced by plasma nitriding in a 316L polycrystalline stainless steel, Acta Mater. 58 (2010) 2814–2821.
[53] C. Templier, J.C. Stinville, P. Villechaise, P.O. Renault, G. Abrasonis, J.P. Riviere, A. Martinavicius, M. Drouet, On lattice plane rotation and crystallographic structure of the expanded austenite in plasma nitrided AISI 316L steel Surf, Coat. Technol. 204 (2010) 2551–2558.
[54] C. Templier, J.C. Stinville, P.O. Renault, G. Abrasonis, P. Villechaise, J.P. Rivière, M. Drouet, Nitrogen interstitial induced texture depth gradient in stainless steel, Scr. Mater. 63 (5) (2010) 496–499.
[55] J.C. Stinville, J. Cormier, C. Templier, P. Villechaise, Modeling of the lattice rotations induced by plasma nitriding of 316L polycrystalline stainless steel, Acta Mater. 83 (2015) 10–16.
[56] S.C. Gallo, H. Dong, New insights into the mechanism of low-temperature active-screen plasma nitriding of austenitic stainless steel, Scr. Mater. 67 (1) (2012) 89–91.
[57] X. Zhang, C.C. da Silva, C. Liu, M. Prabhakar, M. Rohwerder, Selective oxidation of ternary Fe-Mn-Si alloys during annealing process, Corros. Sci. 174 (2020) 108859.
[58] Y.F. Gong, B.C.D. Cooman, Selective oxidation and sub-surface phase transformation of TWIP steel during continuous annealing, Steel Res. Int. 82 (11) (2011) 1310–1318.
[59] L. Cho, B.C.D. Cooman, Selective oxidation of TWIP steel during continuous annealing, Steel Res. Int. 83 (4) (2012) 391–397.
[60] X. Jin, Y. Zhong, L. Wang, H. Wang, Effect of annealing temperature on the surface and subsurface microstructure of Al-added TWIP steel, Surf. Coat. Technol. 386 (2020) 125479.
[61] H. Wang, X. Jin, G. Hu, Y. He, Changing oxide layer structures with respect to the dew point prior to hot-dip galvanizing of δ-TRIP steel, Surf. Coat. Technol. 337 (2018) 260–269.

[62] S. Guruswamy, S.M. Park, J.P. Hirth, R.A. Rapp, Internal oxidation of Ag-in alloys: Stress relief and the influence of imposed strain, Oxid. Met. 26 (1) (1986) 77–100.
[63] C.X. Li, H. Dong, T. Bell, A feasibility study of plasma nitriding of steel with an oxide layer on the surface, J. Mater. Sci. 41 (18) (2006) 6116–6118.
[64] C.X. Li, Active screen plasma nitriding – an overview, Surf. Eng. 26 (1-2) (2010) 135–141.
[65] S. Fritsch, A. Navrotsky, Thermodynamic properties of manganese oxides, J. Am. Ceram. Soc. 79 (7) (1996) 1761–1768.
[66] A.N. Grundy, B. Hallstedt, L.J. Gauckler, Assessment of the Mn-O system, J. Ph. Equilibria 24 (1) (2003) 21–39.
[67] T. Hidayat, D. Shishin, E. Jak, S.A. Decterov, Thermodynamic reevaluation of the Fe–O system, Calphad 48 (2015) 131–144.
[68] K.T. Jacob, A. Kumar, Y. Waseda, Gibbs energy of formation of MnO: measurement and assessment, J. Ph. Equilibria Diffus. 29 (3) (2008) 222–230.
[69] T.K. Jeong, G. Jung, K. Lee, Y.B. Kang, H.K.D.H. Bhadeshia, D.W. Suh, Selective oxidation of Al rich Fe–Mn–Al–C low density steels, Mater. Sci. Technol. 30 (14) (2014) 1805–1814.
[70] P.C. Chen, C.G. Chao, J.Y. Juang, T.F. Liu, Structure and properties of gas-nitrided nanostructured FeAlMnC alloy, Mater. Chem. Phys. 143 (1) (2013) 271–274.
[71] Y.C. Chen, C.L. Lin, C.G. Chao, T.F. Liu, Excellent enhancement of corrosion properties of Fe–9Al–30Mn–1.8C alloy in 3.5% NaCl and 10% HCl aqueous solutions using gas nitriding treatment, J. Alloy. Compd. 633 (2015) 137–144.
[72] S.J. Hsueh, J.Y. Huang, C.G. Chao, J.Y. Juang, T.F. Liu, Mechanical behavior and electrochemical stability of gas-nitrided FeMnAlC alloy in simulated body fluid, Mater. Lett. 216 (2018) 150–153.
[73] I. Olefjord, W. Leijon, U. Jelvestam, Selective surface ace oxidation during annealing of steel sheets in H2/N2, Appl. Surf. Sci. 6 (3) (1980) 241–255.
[74] S. Feliu, M.L. Pérez-Revenga, Effect of the presence of alloying elements in interstitial-free and low-carbon steels on their surface composition after annealing in reducing atmospheres (dew point=−30°C), Metall. Mater. Trans. A 35 (7) (2004) 2039–2050.
[75] X.S. Li, S.I. Baek, C.S. Oh, S.J. Kim, Y.W. Kim, Oxide formation of transformation-induced plasticity-aided steel during dew-point control, Scr. Mater. 57 (2) (2007) 113–116.
[76] X. Jin, G. Hu, H. Qian, H. Wang, Effect of dew point on galvanizability in 4 mass% Al added low density steel, ISIJ Int. 58 (9) (2018) 1584–1591.